

<sup>1</sup>  
<sup>2</sup> Susceptible host dynamics explain pathogen resilience to  
<sup>3</sup> perturbations

<sup>4</sup>  
<sup>5</sup> Sang Woo Park, . . . , Sarah Cobey

## <sup>6</sup> Abstract

<sup>7</sup> Major priority for epidemiological research in the time of anthropogenic change is  
<sup>8</sup> understanding how infectious disease dynamics respond to perturbations. Interven-  
<sup>9</sup> tions to slow the spread of SARS-CoV-2 significantly disrupted the transmission  
<sup>10</sup> of other human pathogens. As interventions lifted, whether and when respiratory  
<sup>11</sup> pathogens would eventually return to their pre-pandemic dynamics remains to be  
<sup>12</sup> answered. To address this gap, we develop a framework for estimating pathogen re-  
<sup>13</sup> silience based on how fast epidemic patterns return to their pre-pandemic, endemic  
<sup>14</sup> dynamics. Our analysis suggests that some pathogens may have settled to endemic  
<sup>15</sup> cycles that are different from their pre-pandemic patterns. Finally, we show that  
<sup>16</sup> the replenishment rate of the susceptible pool is a key determinant of pathogen re-  
<sup>17</sup> silience. Our framework offers a novel perspective to characterizing the dynamics of  
<sup>18</sup> endemic pathogens and their responses to SARS-CoV-2 interventions. [SWP: Need  
<sup>19</sup> to emphasize broader implications.]

20 Non-pharmaceutical interventions (NPIs) to slow the spread of SARS-CoV-2 dis-  
21 rupted the transmission of other human respiratory pathogens, adding uncertainties  
22 to their future epidemic dynamics and the overall public health burden [1]. As in-  
23 terventions lifted, large heterogeneities in outbreak dynamics were observed across  
24 different pathogens in different countries, with some pathogens exhibiting earlier  
25 resurgences than others [2, 3, 4]. Heterogeneities in the overall reduction in trans-  
26 mission and the timing of re-emergence likely reflect differences in NPI patterns,  
27 pathogen characteristics, immigration/importation from other countries, and pre-  
28 pandemic pathogen dynamics; therefore, comparing the differential impact of the  
29 pandemic NPIs across pathogens can provide unique opportunities to learn about  
30 underlying pathogen characteristics, such as their transmissibility or duration of im-  
31 munity, from heterogeneities in re-emergence patterns [5].

32 Even though more than five years have passed since the emergence of SARS-CoV-  
33 2, we still observe persistent changes in pathogen dynamics following the pandemic  
34 NPIs: for example, compared to pre-pandemic, seasonal patterns, human metapneu-  
35 movirus and bocavirus in Korea are circulating at lower levels, whereas RSV in Korea  
36 seem to exhibit different seasonality (Figure 1). These observations suggest a possi-  
37 bility for a fundamental change in pathogen dynamics following the pandemic NPIs,  
38 which can be driven by permanent shift in either human behavior or population-level  
39 immunity [6, 7].

40 Non-pharmaceutical interventions (NPIs) to slow the spread of SARS-CoV-2 dis-  
41 rupted the transmission of other human pathogens, providing large-scale natural  
42 experiments for understanding how various host-pathogen systems respond to per-  
43 turbations [1, 2, 3, 4]. As interventions lifted, large heterogeneities in outbreak  
44 dynamics were observed across different pathogens in different countries (Figure  
45 1), likely reflecting differences in NPI patterns, pathogen characteristics, immigra-  
46 tion/importation from other countries, and pre-pandemic pathogen dynamics [5].  
47 Understanding how different factors contribute to the heterogeneity in re-emergence  
48 patterns has remained a key challenge for predicting future outbreaks, including  
49 whether we will see persistent changes in pathogen dynamics.

50 More than five years have passed since the emergence of SARS-CoV-2, and we  
51 now have potential evidence for persistent changes in pathogen dynamics follow-  
52 ing the pandemic, which likely reflect permanent shift in either human behavior or  
53 population-level immunity [6, 7]. For example, compared to pre-pandemic, seasonal  
54 patterns, human metapneumovirus and bocavirus in Korea are circulating at lower  
55 levels, whereas RSV in Korea seem to exhibit different seasonality (Figure 1). These  
56 observations pose two fundamental questions for current and future infectious dis-  
57 ease dynamics: (1) can we learn about underlying pathogen characteristics, such as  
58 their transmissibility or duration of immunity, from heterogeneities in re-emergence  
59 patterns? and (2) can we predict whether and when other respiratory pathogens will  
60 eventually return to their pre-pandemic dynamics?

61 Understanding how ecological systems respond to perturbations is a fundamental  
62 challenge in predicting population persistence and extinction [8, 9, 10]. These re-

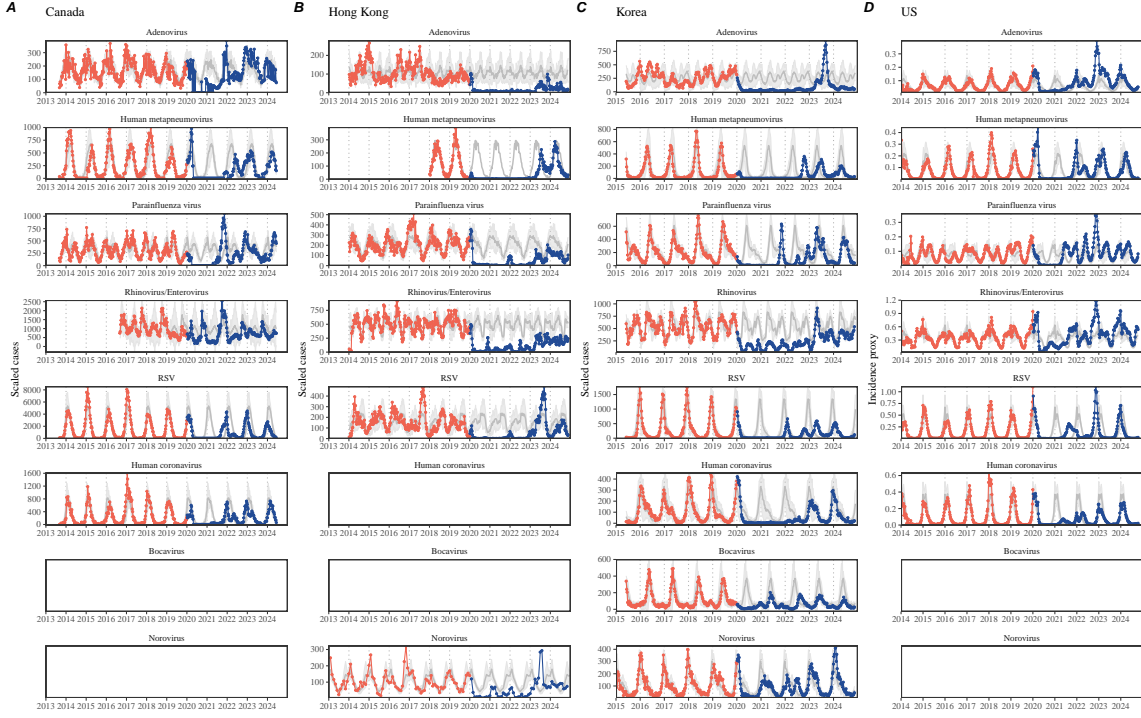


**Figure 1: Observed heterogeneity in responses to COVID-19 pandemic across respiratory pathogens and norovirus in (A) Canada, (B) Hong Kong, (C) Korea, and (D) US.** Red points and lines represent data before 2020. Blue points and lines represent data since 2020. Gray lines and shaded regions represent the mean seasonal patterns and corresponding 95% confidence intervals based on the observed outbreak patterns before 2020.

63 responses can be characterized in terms of resilience, which often measures how fast a  
 64 system returns to its stable, reference state following a perturbation [11, 12, 13, 14].  
 65 Theoretical and empirical efforts to quantify resilience of ecological systems have pro-  
 66 vided key insights for understanding the dynamics of complex systems and linking  
 67 these findings to actionable strategies for species conservation [15]. However, de-  
 68 spite rich literature on ecological resilience, there have been limited applications to  
 69 measuring the resilience of host-pathogen systems, especially for human pathogens.

70 To address this question, we propose a framework for characterizing the resilience  
 71 of a host-pathogen system based on how fast the system recovers from perturbation.  
 72 We begin by laying out a few representative scenarios that capture the potential im-  
 73 pact of COVID-19 interventions on endemic pathogen dynamics and illustrating how  
 74 resilience can be measured by comparing the pre- and post-pandemic dynamics of  
 75 susceptible and infected hosts. In practice, information on susceptible hosts are often  
 76 unavailable, and traditional methods for reconstructing the dynamics of susceptible  
 77 hosts require long-term endemic time series [16, 17], which cannot be applied due  
 78 to disruptions in epidemic patterns caused by COVID-19 interventions. Instead, we

79 utilize Takens' embedding theorem to reconstruct empirical attractors from data and  
80 further measure the distance from this empirical attractor [18]. This reconstruction  
81 allows us to characterize the rate at which this distance decreases over time, which  
82 correspond to pathogen resilience. We apply this framework to analyzing pathogen  
83 surveillance data for a wide array of respiratory and non-respiratory pathogens from  
84 Canada, Hong Kong, Korea, and US. Finally, we show that susceptible host dynamics  
85 are a key determinants of pathogen resilience. Our study offers unique insights into  
86 understanding pathogen re-emergence patterns following COVID-19 interventions.

## 87 Conceptual introduction to pathogen resilience

88 In classical ecological literature, resilience of an ecological system is measured by  
89 the rate at which the system returns to its reference state following a perturbation  
90 [11, 12, 13, 14]. This rate corresponds to the largest real part of the eigenvalues of  
91 the linearized system near equilibrium—here, we refer to this value as the *intrinsic*  
92 resilience of the system, which represents the expected rate of return from perturbed  
93 states. However, respiratory pathogens often exhibit seasonal variation in transmis-  
94 sion, meaning that the intrinsic resilience of a host-pathogen system varies across  
95 season. Nonetheless, we can still measure the *empirical* resilience of a host-pathogen  
96 system by looking at how fast the system returns to the pre-pandemic, endemic  
97 dynamics after interventions are lifted.

98 As an example, consider an intervention that reduce transmission by 50% for 6  
99 months starting in 2020, which causes epidemic patterns to deviate from its original  
100 stable annual cycle for a short period of time and eventually come back (Figure 2A).  
101 To measure the empirical resilience of this system, we first need to be able to measure  
102 the distance from its pre-pandemic attractor. There are many different ways we can  
103 measure the distance from attractor, but for illustrative purposes, we choose one of  
104 the most parsimonious approach: that is, we look at how the susceptible (S) and  
105 infected (I) populations change over time and measure the distance on the SI phase  
106 plane (Figure 2B). In this simple case, the locally estimated scatterplot smoothing  
107 (LOESS) fit indicates that the distance from attractor decreases linearly on average  
108 (Figure 2C). Furthermore, the overall rate of return matches the intrinsic resilience  
109 of the seasonally unforced system (Figure 2C).

110 Alternatively, NPIs can permanently change our behavior and have persisting  
111 impact on the pathogen dynamics; as an example, we consider a scenario in which a  
112 10% reduction in transmission persists even after the NPIs are lifted (Figure 2D–F).  
113 In such cases, we cannot know whether the pathogen will return to its original cycle  
114 or a different cycle until many years have passed after the NPIs are lifted, meaning  
115 that we cannot measure the distance against the new attractor that the system will  
116 eventually approach. Nonetheless, we can still measure the distance against the orig-  
117 inal, pre-pandemic attractor and ask how the distance changes over time (Figure 2E).  
118 The LOESS fit suggests that the distance from the attractor will initially decrease

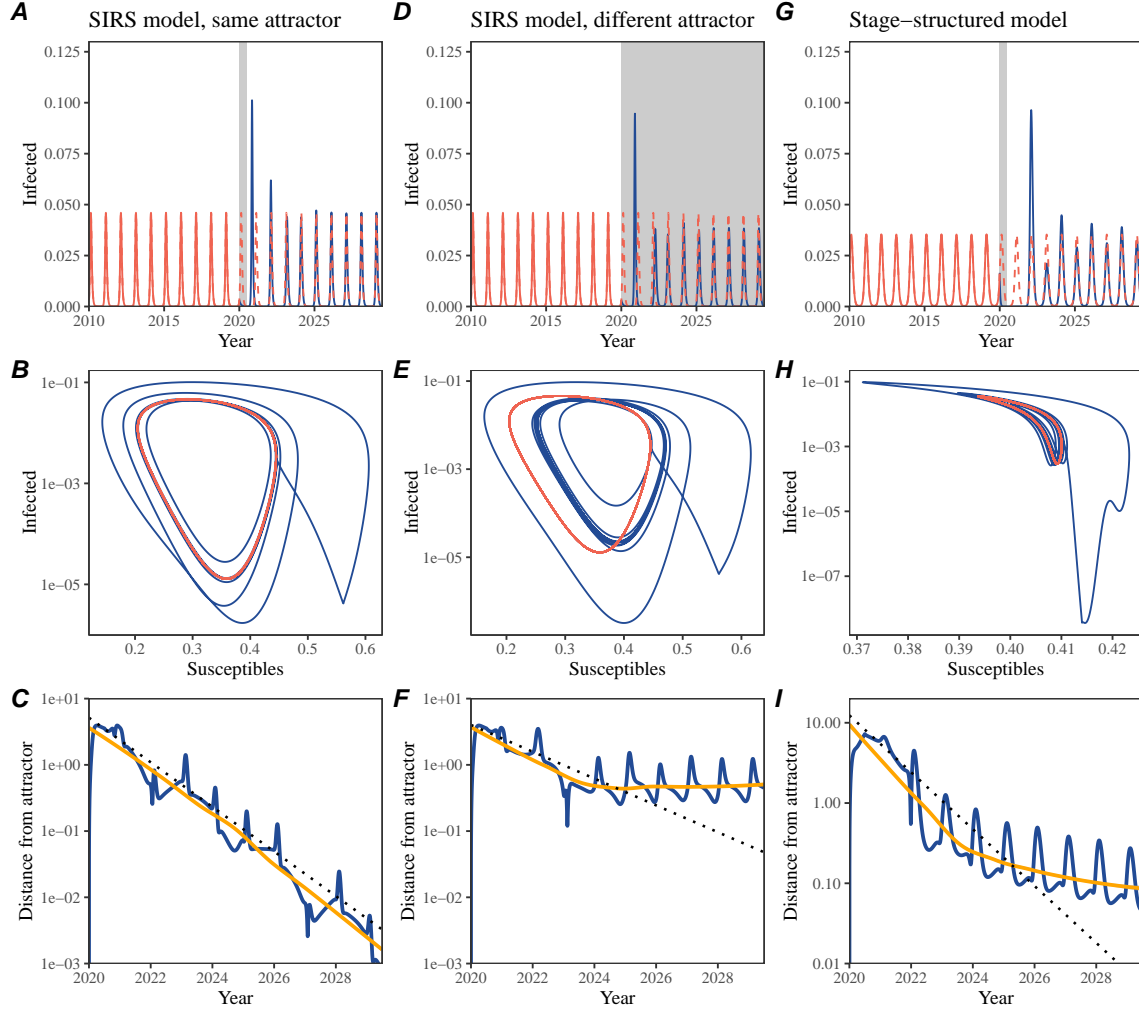


**Figure 2: Conceptual framework for measuring pathogen resilience following NPIs across different scenarios.** (A, D, G) Simulated epidemic trajectories across various models. Red and blue solid lines represent epidemic dynamics before and after interventions are introduced, respectively. Red dashed lines represent counterfactual epidemic dynamics in the absence of interventions. Gray regions indicate the duration of interventions. (B, E, H) Phase plane representation of the corresponding model. Red and blue solid lines represent epidemic trajectories on an SI phase plane before and after interventions are introduced, respectively. (C, F, I) Changes in logged distance from attractor over time. Blue lines represent the logged distance from attractor. Orange lines represent the locally estimated scatterplot smoothing (LOESS) fits to the logged distance from attractor. Dotted lines are superimposed as a comparison to have the same slope as the intrinsic resilience of the seasonally unforced system.

119 exponentially on average (equivalently, linearly on a log scale) and eventually plateau

(Figure 2F). Here, a permanent 10% reduction in transmission rate slows down the system, which causes the distance from the attractor to decrease at a slower rate (Figure 2F) than it would have otherwise in the absence of permanent transmission reduction (Figure 2C). This example shows that resilience is not necessarily an intrinsic property of a specific pathogen. Instead, pathogen resilience is a property of a specific attractor that a host-pathogen system approaches, which depends on both pathogen and host characteristics.

Finally, transient phenomena can also complicate the picture (Figure 2G–I). For example, a stage-structured model for RSV initially exhibits a stable annual cycle, but perturbations from NPIs cause the epidemic to exhibit biennial cycles (Figure 2G). Despite this biennial cycle, we see that the system eventually approaches the original pre-pandemic attractor (Figure 2H), suggesting that this biennial cycle is a transient phenomenon. The LOESS fit indicates that the distance from the attractor will initially decrease exponentially at a rate that is consistent with the intrinsic resilience of the seasonally unforced system, but the rate of decrease slows down as the epidemic exhibits a biennial cycle (Figure 2I). In classical ecological theory, this behavior is also referred to as a ghost attractor, which causes long transient dynamics and slow transitions [19]. As we show in Supplementary Figure S1, strong seasonal forcing in transmission can also lead to transient phenomena for a simple SIRS model, causing a slowing down of the system.

In Supplementary Materials, we also explore measuring the resilience of a two-strain host-pathogen system: when the dynamics two strains (or two pathogens) are coupled through cross immunity, we would expect the entire system to be characterized by a single resilience value (rather than having two separate resilience for each strain). Simulations from a simple two-strain system illustrate that separate analyses of individual strain dynamics (e.g., RSV A vs B) and a joint analysis of total infections (e.g., total RSV infections) yield identical resilience estimates, confirming our expectation (Supplementary Figure S2, 3). Analogous to a single system, strong seasonal forcing in transmission can cause the system to slow down through transient phenomena (Supplementary Figure S4).

These observations indicate three possibilities. First, we can directly estimate the empirical resilience of a host-pathogen system by looking at how fast the system approaches a pre-pandemic attractor, provided that we can measure the distance from attractor. The empirical approach to estimating pathogen resilience is particularly convenient because it does not require us to know the true underlying model. As we show in Supplementary Figure S5, estimating the intrinsic resilience from fitting standard compartmental models can lead to biased estimates, especially under model misspecification. Second, resilience estimates allow us to make phenomenological predictions about the dynamics of a host-pathogen system following a perturbation: assuming that the distance from the attractor will decrease exponentially over time, we can obtain a ballpark estimate for when the system will reach an attractor. Finally, deviation from an exponential decrease in the distance from attractor can provide information about whether the system has reached an alternative attractor,

163 or a ghost attractor, that is different from the original, pre-pandemic attractor. These  
164 alternative attractors may reflect continued perturbations from permanent changes  
165 in transmission patterns as well as changes in immune landscapes.

## 166 Inferring pathogen resilience from real data

167 Based on these observations, we now set out to infer pathogen resilience from real  
168 data. Here, we briefly lay out our approach to estimating pathogen resilience from  
169 real data (Figure 3). We then test this approach against simulations and apply it to  
170 real data.

171 So far, we focused on simple examples that assume a constant transmission re-  
172 duction. However, in practice, the impact of NPIs on pathogen transmission is  
173 likely more complex (Figure 3A), reflecting introduction and relaxation of various  
174 intervention strategies. These complexities can lead to longer delays between the  
175 introduction of NPIs and pathogen re-emergence as well as temporal variation in  
176 outbreak sizes (Figure 3B): in this example, continued transmission reduction from  
177 NPIs limits the size of the first outbreak in 2021 following the emergence, allowing  
178 for a larger outbreak in 2022 when NPIs are further relaxed.

179 Previously, we relied on the dynamics of susceptible and infected hosts to compute  
180 the distance from attractor (Figure 2), but information on susceptible hosts are  
181 often not available in practice. In addition, uncertainties in case counts due to  
182 observation error as well as the possibility of complex, multiannual attractor adds  
183 challenges to measuring the distance from attractor. To address these challenges, we  
184 first reconstruct an empirical attractor by utilizing Takens' theorem, which states  
185 that an attractor of a nonlinear multidimensional system can be mapped onto a  
186 delayed embedding [18]. Here, we use delayed copies of logged values of pre-pandemic  
187 cases  $C(t)$  (Figure 3C) to reconstruct the attractor:

$$\langle \log(C(t) + 1), \log(C(t - \tau) + 1), \dots, \log(C(t - (M - 1)\tau) + 1) \rangle, \quad (1)$$

188 where the delay  $\tau$  and embedding dimension  $M$  are determined based on autocor-  
189 relations and false nearest neighbors, respectively [20, 21]. We then apply the same  
190 delay and embedding dimensions to the entire time series to determine the position  
191 on a multi-dimensional state space (Figure 3D), which allows us to measure the  
192 nearest neighbor distance between the current state of the system and the empirical  
193 attractor (Figure 3E). In principle, we can quantify how fast this distance decreases  
194 by fitting a linear regression on a log scale, where the slope of the linear regression  
195 corresponds to pathogen resilience. As we show in Supplementary Figure S6, over-  
196 all temporal variations in the distance from attractor, especially the observed rate  
197 of decrease, appear robust to choices about embedding delays and dimensions; we  
198 note that using longer delays and higher dimensions tend to smooth out temporal  
199 variations in the distance from attractor.

200 Complex changes in the distance from attractor suggest that estimating pathogen  
201 resilience from linear regression will likely be sensitive to our choice of fitting windows

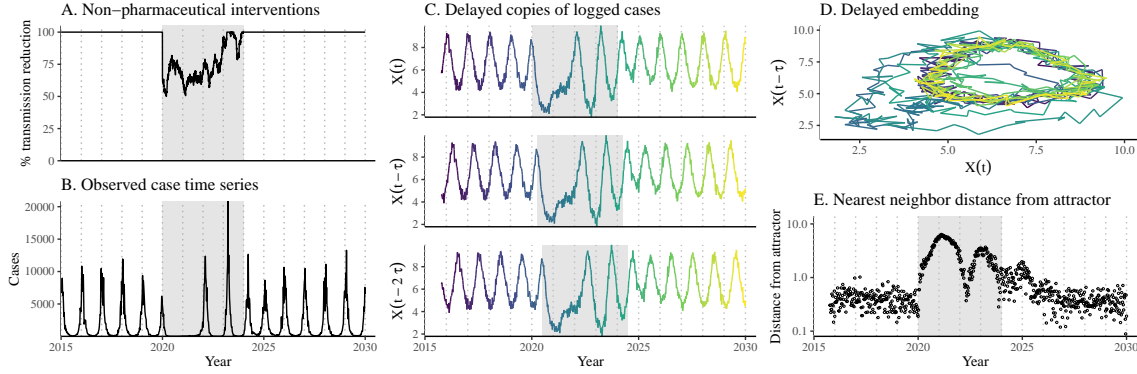
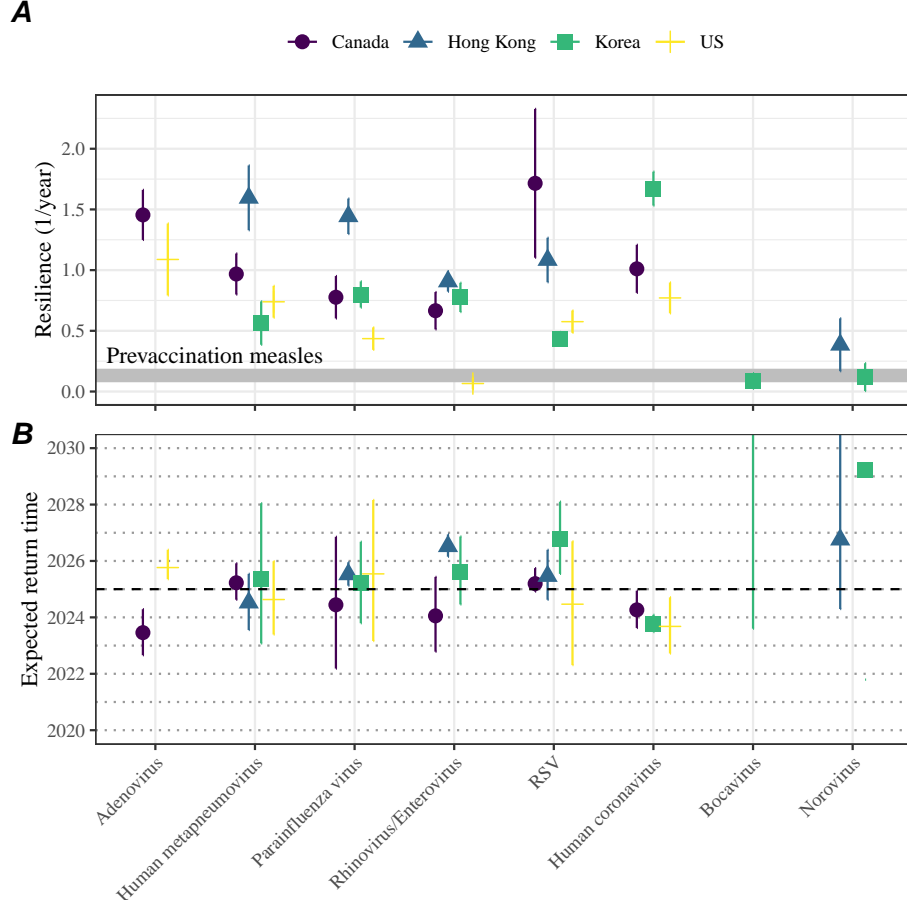


Figure 3: **A schematic diagram explaining how pathogen resilience can be inferred from real data.** (A) A realistic example of a synthetic NPI, represented by a relative reduction in transmission. (B) The impact of the synthetic NPI on epidemic dynamics simulated using a stochastic SIRS model. (C) Generating delayed copies of the logged time series allows us to obtain an embedding. (D) Two dimensional representation of an embedding. (E) Delayed embedding allows us to calculate the nearest neighbor distance from the empirical attractor, which is determined based on the pre-pandemic time series. This distance time series can be used to infer pathogen resilience by fitting a linear regression after choosing an appropriate window for regression.

for the regression. In Supplementary Materials, we explore an automated window selection criteria for linear regression and test it against randomized, stochastic simulations across a wide range of realistic NPI shapes. We find that resilience estimates based on the automated window selection criteria are moderately correlated (0.48) with the intrinsic resilience of the post-NPI attractor (Supplementary Figure S7). In contrast, a naive approach that uses the entire time series, starting from the peak distance, only gives a correlation of 0.09 and consistently underestimates the intrinsic resilience (Supplementary Figure S7).

Now, we apply this approach to pathogen surveillance data presented in Figure 1. For each time series, we apply Takens' theorem independently to reconstruct the empirical attractor and obtain the corresponding time series of distance from attractors (Supplementary Figure S8 for the distance time series and linear regression fits). Then, we use the automated window selection criteria to fit a linear regression and estimate the empirical resilience for each pathogen in each country. For most respiratory pathogens, resilience estimates fall between 0.4/year and 1.8/year (Figure 4A), with the exception of Rhinovirus in the US (0.066/year; 95% CI: 0.018/year–0.113/year) and Bocavirus in Korea (0.087/year; 95% CI: 0.023/year–0.151/year). Excluding these exceptions, the mean resilience of common respiratory pathogens is 0.974/year (95% CI: 0.784/year–1.16/year). As a reference, this is  $\approx 7$  times higher than the intrinsic resilience of pre-vaccination measles dynamics ( $\approx 0.13/\text{year}$ ). Finally, resilience estimates for norovirus appears to be comparable to the intrinsic

resilience of measles: 0.119/year (95%CI: 0.004/year–0.233/year) for Korea and 0.385/year (95% CI: 0.167/year–0.603/year). A simple ANOVA shows that there are significant differences in resilience estimates across countries ( $p < 0.036$ ) and pathogens ( $p < 0.030$ ).



**Figure 4: Summary of resilience estimates.** (A) Estimated pathogen resilience. The gray horizontal line represents the intrinsic resilience of pre-vaccination measles dynamics. (B) Predicted timing of when each pathogen will return to their pre-pandemic cycles. The dashed line in panel B indicates the end of 2024 (current observation time). Error bars represent 95% confidence intervals.

Using resilience estimates, we now predict when each pathogen will return to their original pre-pandemic cycles. Specifically, we extend our linear regression fits to distance-from-attractor time series and ask when the predicted regression line will cross a threshold value, which we set to a mean of pre-pandemic distances. We predict that a return to pre-pandemic cycles would be imminent for most pathogens (Figure 4B; see Supplementary Figure S9 for a zoomed out version). In addition, we also predict that many pathogens should have already returned to their pre-pandemic

234 dynamics by the end of 2024; but these predictions contradict some of the observed  
235 pathogen dynamics. For example, we predict that both human metapneumovirus and  
236 RSV in Korea should have returned to their attractors by now, but the magnitude  
237 and timing of recent epidemics are different from pre-pandemic patterns (Figure 1).  
238 These observations suggest the possibility that some common respiratory pathogens  
239 may have converged to different attractors.

240 In Supplementary Materials, we also consider using a lower threshold for the false  
241 nearest neighbor approach when determining the embedding dimension; this gives  
242 a higher embedding dimension. As explained earlier (Supplementary Figure S6),  
243 this gives a smoother distance-from-attractor time series (compare Supplementary  
244 Figure S10 with S8); this also requires us to use longer time series, which prevents  
245 us from estimating resilience for some pathogens. Overall, resulting estimates of  
246 pathogen resilience with higher embedding dimensions still fall between 0.3/year  
247 and 2.1/year for the most part (Supplementary Figure S11). A direct comparison  
248 between two approaches (i.e., original estimate vs using higher dimensions) shows a  
249 strong consistency in resilience estimates (Supplementary Figure S12).

## 250 **Susceptible host dynamics explain variation in pathogen 251 resilience**

252 So far, we focused on quantifying pathogen resilience from the observed patterns of  
253 pathogen re-emergence following COVID-19 interventions. But what factors deter-  
254 mine how resilient a host-pathogen system is? Here, we use a standard Susceptible-  
255 Infected-Recovered-Susceptible (SIRS) model to show that susceptible host dynamics  
256 are the key determinants of pathogen resilience. To do so, we vary the basic reproduc-  
257 tion number  $\mathcal{R}_0$ , which represents the average number of secondary infections caused  
258 by a newly infected individual in a fully susceptible population, and the duration of  
259 immunity and compute intrinsic resilience for each parameter.

260 We find an increase in  $\mathcal{R}_0$  and a decrease in duration of immunity correspond  
261 to an increase in pathogen resilience (Figure 5A). These variations can be under-  
262 stood in terms of the susceptible host dynamics, where faster per-capita suscepti-  
263 ble replenishment rate causes the system to be more resilient (Figure 5B). This rate can  
264 be expressed as a ratio between absolute rate at which new susceptibles enter the  
265 population and the equilibrium number of susceptible individuals in the population,  
266  $\bar{S}$ . Therefore, both higher  $\mathcal{R}_0$  and shorter duration of immunity can drive faster  
267 per-capita susceptible replenishment rate (Figure 5B), especially because higher  $\mathcal{R}_0$   
268 leads to lower  $\bar{S}$ .

269 Finally, we can now rank different pathogens based on the average values of em-  
270 pirical resilience, which allows us to determine a set of parameters that are consistent  
271 with the estimated resilience (Figure 5A). Across all pathogens we consider, except  
272 for bocavirus and norovirus, we estimate that the average duration of immunity is  
273 likely to be short (< 6 years) across a plausible range of  $\mathcal{R}_0$ . These rankings further

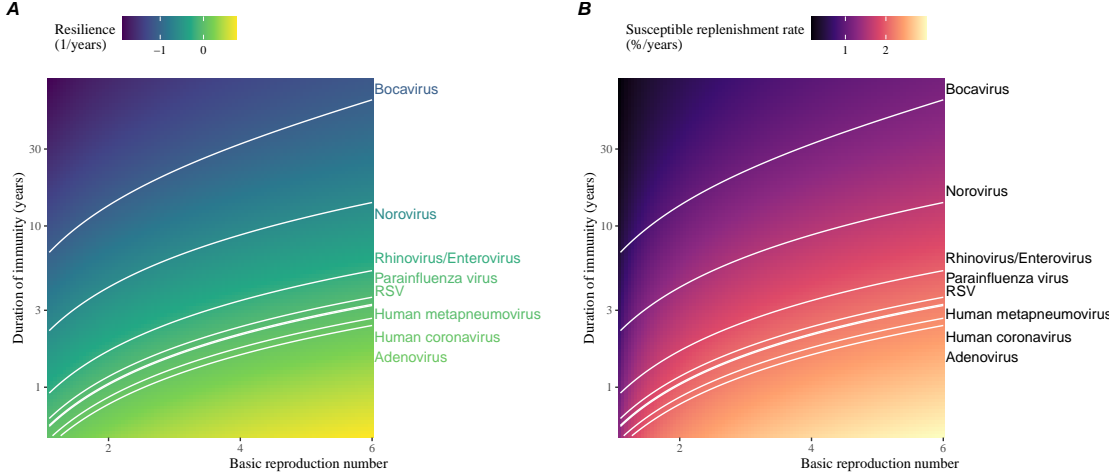


**Figure 5: Linking pathogen resilience to epidemiological parameters and susceptible host dynamics.** (A) The heat map represents intrinsic resilience as a function of the basic reproduction number  $\mathcal{R}_0$  and the duration of immunity. (B) The heat map represents per-capita susceptible replenishment rate as a function of the basic reproduction number  $\mathcal{R}_0$  and the duration of immunity. The standard SIRS model is used to compute intrinsic resilience and per-capita susceptible replenishment rate. Lines correspond to a set of parameters that are consistent with mean resilience estimates for each pathogen. Pathogens are ranked based on their mean resilience estimates, averaged across different countries.

allow us to map each pathogen onto a set of parameters that are consistent with its empirical resilience (Figure 5A) and obtain a plausible range of susceptible replenishment rates for each pathogen (Figure 5B). However, we note that there is no one-to-one correspondence between susceptible replenishment rates and pathogen resilience, leading to a wide uncertainty in the estimates for susceptible replenishment rates (Figure 5B).

## Discussion

The COVID-19 interventions have caused major disruptions to circulation patterns of both respiratory and non-respiratory pathogens, adding challenges to predicting their future dynamics [1, 2, 3, 4]. On the other hand, these interventions offer large-scale natural experiments for understanding how different pathogens respond to perturbations. In this study, we show that pathogen re-emergence patterns following COVID-19 interventions can be characterized through the lens of ecological resilience. Traditionally, ecological resilience measures how fast a system returns to a reference state following a perturbation. In the context of respiratory pathogens, resilience measures how fast epidemics return to their endemic cycles after interventions are

290 lifted.

291 We use an attractor reconstruction approach to quantify how distance from at-  
292 tractor changes over time for each pathogen [18]. We show that the resilience of  
293 a host-pathogen system can be estimated by fitting a linear regression to a logged  
294 distance-from-attractor time series. Overall, we estimate that the resilience for most  
295 common respiratory pathogens ranges between 0.4/year and 1.8/year, which is 3–14  
296 times more resilient than prevaccination measles, indicating potential challenges in  
297 controlling common respiratory pathogens.

298 Our framework allows us to make phenomenological predictions about when each  
299 pathogen will return to their endemic cycles. The ability to predict future epidemic  
300 patterns from resilience estimates offers a new paradigm for epidemic forecasting.  
301 While this approach cannot predict the exact timing of outbreaks or epidemic pat-  
302 terns, it is nonetheless useful for predicting when epidemics will settle down to regular  
303 cycles after a large perturbation, such as COVID-19 interventions.

304 Our analyses suggest a possibility that several pathogens may have converged  
305 to different endemic cycles compared to their pre-pandemic epidemic patterns. Key  
306 examples include human metapnuemovirus, RSV, and bocavirus in Korea as well as  
307 RSV in Hong Kong. These changes may reflect changes in surveillance or actual shift  
308 in the dynamics, caused by permanent changes in behavior or population-level immu-  
309 nity. While it seems unlikely that permanent changes in behavior would only affect a  
310 few pathogens and not others, we cannot rule out this possibility given heterogeneity  
311 in the age of infection across different respiratory pathogens [SWP: CITE]. A shift  
312 in population-level immunity is plausible, as the emergence of SARS-CoV-2 and ex-  
313 tinction of influenza B/Yamagata likely caused major changes in immune landscapes;  
314 interactions among co-circulating pathogens, such as cross immunity between RSV  
315 and HMPV [22], may have also contributed to changes in population-level immu-  
316 nity. However, we currently do not know how immunity, or lack thereof, from these  
317 pathogens would affect infection from other pathogens. Future studies should use  
318 detailed mechanistic models, coupled with behavioral and immunological data, to  
319 test these hypotheses and better understand post-pandemic dynamics of endemic  
320 pathogens.

321 We show that susceptible host dynamics shape pathogen resilience, where faster  
322 replenishment of the susceptible population causes the pathogen to be more resilient.  
323 For simplicity, we focus on waning immunity and birth as a main driver of the suscep-  
324 tible host dynamics but other mechanisms can also contribute to the replenishment  
325 of the susceptible population. In particular, pathogen evolution, especially the emer-  
326 gence of antigenically novel strains, can cause effective waning of immunity in the  
327 population; therefore, we hypothesize that faster rates of antigenic evolution can also  
328 cause a pathogen to be more resilient. Future studies should explore the relationship  
329 between the rate of evolution and resilience for antigenically evolving pathogens.

330 Quantifying pathogen resilience also offers novel approaches to validating population-  
331 level epidemiological models. So far, the majority of model validation in epidemiology  
332 is based on the ability of a model to reproduce the observed epidemic dynamics and

333 to predict future dynamics [23, 22, 24, 25, 26]. However, there can be plethora of  
334 models that meet these criteria. For example, two major RSV models have been pro-  
335 posed so far to explain biennial epidemic patterns: (1) a stage- and age-structured  
336 model that allows for disease severity to vary with number of past infections and  
337 age of infection [24] and (2) a pathogen-interaction model that accounts for cross  
338 immunity between RSV and human metapnuemovirus [22]. Since both models can  
339 accurately reproduce the observed epidemic patterns, standard criteria for model  
340 validation do not allow us to distinguish between these two models from population-  
341 level data alone. Instead, we can measure the empirical resilience of each model  
342 by simulating various perturbations and compare them to estimates of empirical re-  
343 silience from data, using COVID-19 interventions as an opportunity. Future studies  
344 should further investigate using pathogen resilience for validating epidemic models.

345 There are several limitations to our work. First of all, we did not extensively ex-  
346 plore other approaches to reconstructing the attractor. Recent studies showed that  
347 more sophisticated approaches, such as using non-uniform embedding, can provide  
348 more robust reconstruction for noisy data [21]. In the context of causal inference,  
349 choices about embedding can have major impact on the resulting inference [27]. Our  
350 resilience estimates are likely overly confident given a lack of uncertainties in at-  
351 tractor reconstruction as well as the simplicity of our statistical framework. Short  
352 pre-pandemic time series also contributes to the crudeness of our estimates. Nonethe-  
353 less, as illustrated in our sensitivity analyses (Supplementary Figure S6, S10–S12),  
354 inferences about pathogen resilience appear to be robust to decisions about embed-  
355 ding lags and dimensions—this is because tracking the rate at which the system  
356 approaches the attractor is likely a much simpler problem than making inferences  
357 about causal directionality. Our qualitative prediction that common respiratory  
358 pathogens are more resilient than prevaccination measles is also likely to be robust  
359 to these predictions, given how rapid many respiratory pathogens returned to their  
360 original cycles following COVID-19 interventions.

361 Predicting the impact of anthropogenic changes on infectious disease dynam-  
362 ics is a fundamental aim of infectious disease research in a rapidly changing world.  
363 Our study illustrates that quantifying pathogen resilience can help us understand  
364 how infectious disease pathogens respond to major perturbations caused by public  
365 health interventions. More broadly, a detailed understanding of the determinants of  
366 pathogen resilience may offer unique insights into pathogen persistence and control-  
367 lability.

## 368 Materials and Methods

### 369 Data

370 We gathered time series on respiratory infections from four different countries: Canada,  
371 Hong Kong, Korea, and United States (US). As a reference, we also included time  
372 series data on norovirus infections for available countries—in contrast to respiratory

373 pathogens, we expect gastrointestinal viruses, such as norovirus, to be less affected  
374 by COVID-19 intervention measures. For all time series, we rounded every year to  
375 52 weeks by taking the average number of cases and tests between the 52nd and  
376 53rd week. We also rescale all time series to account for changes in testing patterns,  
377 which are then used for the actual analysis.

378 Weekly time series of respiratory infection cases in Canada comes from the Res-  
379piratory Virus Detection Surveillance System, which collect data from select lab-  
380oratories across Canada. We extract the data from <https://www.canada.ca/en/public-health/services/surveillance/respiratory-virus-detections-canada.html>. To account for an increase in testing from 2013 to 2024, we calculate a 2 year  
383 moving average for the number of tests for each pathogen, which we use as a proxy  
384 for testing effort. Then, we divide the smoothed testing patterns by the smoothed  
385 value at the final week such that the testing effort has a maximum of 1. We then  
386 divide weekly cases by the testing effort to obtain a scaled case time series. A similar  
387 approach was used earlier for the analysis of RSV time series in the US [24].

388 Weekly time series of respiratory infection cases in Hong Kong comes from the  
389 Centre for Health Protection, Department of Health. We extract the data from  
390 <https://www.chp.gov.hk/en/statistics/data/10/641/642/2274.html>. We also  
391 apply the same scaling procedure to the time series as we did for Canada. For Hong  
392 Kong, we only adjust for testing efforts up to the end of 2019 because there was a  
393 major reduction in testing for common respiratory pathogens since 2020.

394 Weekly time series of acute respiratory infection cases in Korea comes from Ko-  
395 rea Disease Control and Prevention Agency. We extract the data from <https://dportal.kdca.go.kr/pot/is/st/ari.do>. While we do not have information on  
396 testing, the reported number of respiratory infections consistently increased from  
397 2013 to the end of 2019, which we interpreted as changes in testing patterns. Since  
398 we do not have testing numbers, we used the weekly sum of all acute respiratory vi-  
399 ral infection cases as a proxy for testing, which were further smoothed with moving  
400 averaged and scaled to have a maximum of 1. For Korea, we also only adjust for  
401 testing efforts up to the end of 2019.

402 Finally, weekly time series of respiratory infection cases in the US comes from  
403 the National Respiratory and Enteric Virus Surveillance System. In the US, there  
404 has been a large increase in testing against some respiratory pathogens, especially  
405 RSV, which could not be corrected for through simple scaling. Instead, we derive an  
406 incidence proxy by multiplying the test positivity with influenza-like illness positivity,  
407 which is taken from <https://gis.cdc.gov/grasp/fluvview/fluportaldashboard.html>. This method of estimating an incidence proxy has been recently applied in  
408 the analysis of seasonal coronaviruses [6] and Mycoplasma pneumoniae infections [4].  
409 Detailed assumptions and justifications are provided in [28].

412 **Estimating pathogen resilience**

413 In order to measure pathogen resilience from surveillance data, we first reconstruct  
 414 the empirical pre-pandemic attractor of the system using Takens' embedding theorem  
 415 [18]. Specifically, for a given pathogen, we take the pre-pandemic (before 2020)  
 416 case time series  $C(t)$  and reconstruct the attractor using delayed embedding with a  
 417 uniform delay of  $\tau$  and dimension  $M$ :

$$X_{\tau,m}(t) = \langle \log(C(t) + 1), \log(C(t - \tau) + 1), \dots, \log(C(t - (M - 1)\tau) + 1) \rangle. \quad (2)$$

418 Here, the delay  $\tau$  is determined by looking at the autocorrelation of the logged pre-  
 419 pandemic time series and asking when the autocorrelation crosses 0 for the first time  
 420 [21]; a typical delay for an annual outbreak is around 13 weeks.

421 Then, for a given delay  $\tau$ , we determine the embedding dimension  $M$  using the  
 422 false nearest neighbors approach [20, 21]. To do so, we start with an embedding  
 423 dimension  $e$  and construct a set of points  $A_{\tau,e} = \{X_{\tau,e}(t) | t < 2020\}$ . Then, for  
 424 each point  $X_{\tau,e}(t)$ , we determine the nearest neighbor from the set  $A_{\tau,e}$ , which we  
 425 denote  $X_{\tau,e}(t_{nn})$  for  $t \neq t_{nn}$ . Then, if the distance between these two points on  $e + 1$   
 426 dimension,  $D_{\tau,e+1}(t) = \|X_{\tau,e+1}(t_{nn}) - X_{\tau,e+1}(t)\|_2$ , is larger than their distance on  
 427  $e$  dimension,  $D_{\tau,e}(t) = \|X_{\tau,e}(t_{nn}) - X_{\tau,e}(t)\|_2$ , these two points are deemed to be  
 428 false nearest neighbors; specifically, we use a threshold  $R$  for the ratio between two  
 429 distances  $D_{\tau,e+1}(t)/D_{\tau,e}(t)$  to determine false nearest neighbors. In the main text,  
 430 we determine embedding dimension based as the first dimension without any false  
 431 nearest neighbors for  $R = 10$ . In Supplementary Materials, we impose  $R = 5$  to select  
 432 for higher dimensions. Once we determine the embedding lag  $\tau$  and dimension  $M$ ,  
 433 we apply the embedding to the entire time series and calculate the nearest neighbor  
 434 distance against the attractor  $A_{\tau,M}$  to obtain a time series of distance from attractor  
 435  $D_{\tau,M}(t)$ .

436 From a time series of distance from attractor, we estimate pathogen resilience  
 437 by fitting a linear regression to an appropriate window. To automatically select  
 438 the fitting window, we begin by smoothing the distance time series using locally  
 439 estimated scatterplot smoothing (LOESS) to obtain  $\hat{D}_{\tau,M}(t)$ , where the smoothing  
 440 is performed on a log scale and exponentiated afterwards. Then, we determine  
 441 threshold values ( $T_{\text{start}}$  and  $T_{\text{end}}$ ) for the smoothed distances and choose the fitting  
 442 window based on when  $\hat{D}_{\tau,M}(t)$  crosses these threshold values for the first time.  
 443 These thresholds are determined by first calculating maximum distance,

$$\max \hat{D} = \max \hat{D}_{\tau,M}(t), \quad (3)$$

444 and mean pre-pandemic distance,

$$\hat{D}_{\text{mean}} = \frac{1}{N_{t < 2020}} \sum_{t < 2020} \hat{D}_{\tau,M}(t), \quad (4)$$

445 as a reference, and then dividing their ratios into 10 equal bins:

$$T_{\text{start}} = \hat{D}_{\text{mean}} \times \left( \frac{\max \hat{D}}{\hat{D}_{\text{mean}}} \right)^{9/10} \quad (5)$$

$$T_{\text{end}} = \hat{D}_{\text{mean}} \times \left( \frac{\max \hat{D}}{\hat{D}_{\text{mean}}} \right)^{1/10} \quad (6)$$

446 This allows us to discard the initial period during which the distance increases (from  
447 the introduction of intervention measures) and the final period during which the  
448 distance plateaus (as the system reaches an attractor). The fitting window is deter-  
449 mined based on when the smoothed distance  $\hat{D}_{\tau,M}(t)$  crosses these threshold values  
450 for the first time; then, we fit a linear regression to logged (unsmoothed) distances  
451  $\log D_{\tau,M}(t)$  using that window.

## 452 Mathematical modeling

453 Throughout the paper, we use a series of mathematical models to illustrate the con-  
454 cept of pathogen resilience and to understand the determinants of pathogen resilience.  
455 In general, the intrinsic resilience for a given system is given by the largest real part  
456 of the eigenvalues of the linearized system at endemic equilibrium. Here, we focus on  
457 the SIRS model and present the details of other models in Supplementary Materials.  
458 The SIRS (Susceptible-Infected-Recovered-Susceptible) model is the simplest model  
459 that allows for waning of immunity, where recovered (immune) individuals are as-  
460 sumed to become fully susceptible after an average of  $1/\delta$  time period. The dynamics  
461 of the SIRS model is described by the following set of differential equations:

$$\frac{dS}{dt} = \mu - \beta(t)SI - \mu S + \delta R \quad (7)$$

$$\frac{dI}{dt} = \beta(t)SI - (\gamma + \mu)I \quad (8)$$

$$\frac{dR}{dt} = \gamma I - (\delta + \mu)R \quad (9)$$

$$(10)$$

462 where  $\mu$  represents the birth/death rate,  $\beta(t)$  represents the time-varying trans-  
463 mission rate, and  $\gamma$  represents the recovery rate. The basic reproduction number  
464  $\mathcal{R}_0 = \beta(t)/(\gamma + \mu)$  is defined as the average number of secondary infections caused  
465 by a single infected individual in a fully susceptible population and measures the  
466 intrinsic transmissibility of a pathogen.

467 When we first introduce the idea of pathogen resilience (Figure 2), we impose  
468 sinusoidal changes to the transmission rate to account for seasonal transmission:

$$\beta(t) = b_1(1 + \theta \cos(2\pi(t - \phi)))\alpha(t), \quad (11)$$

469 where  $b_1$  represents the baseline transmission rate,  $\theta$  represents the seasonal amplitude,  
 470 and  $\phi$  represents the seasonal offset term. Here, we also introduce an extra  
 471 multiplicative term  $\alpha(t)$  to account for the impact of COVID-19 interventions, where  
 472  $\alpha(t) < 1$  indicates transmission reduction. Figure 2A and 2B are generated assuming  
 473  $b_1 = 3 \times (365/7 + 1/50)/\text{years}$ ,  $\theta = 0.2$ ,  $\phi = 0$ ,  $\mu = 1/50/\text{years}$ ,  $\gamma = 365/7/\text{years}$ , and  
 474  $\delta = 1/2/\text{years}$ . In Figure 2A, we impose a 50% transmission reduction for 6 months  
 475 from 2020:

$$\alpha(t) = \begin{cases} 0.5 & 2020 \leq t < 2020.5 \\ 1 & \text{otherwise} \end{cases} \quad (12)$$

476 In Figure 2B, we impose a 50% transmission reduction for 6 months from 2020 and  
 477 a permanent 10% reduction onward:

$$\alpha(t) = \begin{cases} 1 & t < 2020 \\ 0.5 & 2020 \leq t < 2020.5 \\ 0.9 & 2020.5 \leq t \end{cases} \quad (13)$$

478 In both scenarios, we simulate the SIRS model from the following initial conditions  
 479 ( $S(0) = 1/\mathcal{R}_0$ ,  $I(0) = 1 \times 10^{-6}$ , and  $R(0) = 1 - S(0) - I(0)$ ) from 1900 until 2030.

480 To measure the empirical resilience of the SIR model (Figure 2C and 2F), we  
 481 compute the normalized distance between post-intervention susceptible and logged  
 482 infected proportions and their corresponding pre-intervention values at the same time  
 483 of year:

$$\sqrt{\left(\frac{S(t) - S_{\text{pre}}(t)}{\sigma_S}\right)^2 + \left(\frac{\log I(t) - \log I_{\text{pre}}(t)}{\sigma_{\log I}}\right)^2}, \quad (14)$$

484 where  $\sigma_S$  and  $\sigma_{\log I}$  represent the standard deviation in the pre-intervention suscep-  
 485 tible and logged infected proportions. We normalize the differences in susceptible  
 486 and logged infected proportions to allow both quantities to equally contribute to the  
 487 changes in distance from attractor. In Supplementary Materials, we also compare  
 488 the how the degree of seasonal transmission affects empirical resilience by varying  
 489  $\theta$  from 0 to 0.4; when we assume no seasonality ( $\theta = 0$ ), we do not normalize the  
 490 distance because the standard deviation of pre-intervention dynamics are zero.

491 Finally, we use the SIRS model to understand how underlying epidemiological  
 492 parameters affect pathogen resilience and link this relationship to underlying sus-  
 493 ceptible host dynamics. For the simple SIRS model without seasonal transmission  
 494 ( $\theta = 0$ ), the intrinsic resilience corresponds to:

$$-\frac{\text{Re}(\lambda)}{2} = \frac{\delta + \beta I^* + \mu}{2}. \quad (15)$$

495 Here,  $I^*$  represents the prevalence values at endemic equilibrium:

$$I^* = \frac{(\delta + \mu)(\beta - (\gamma + \mu))}{\beta(\delta + \gamma + \mu)}. \quad (16)$$

<sup>496</sup> The susceptible replenishment rate is given by:

$$S_{\text{replenish}} = \frac{\mu + \delta R}{S^*}, \quad (17)$$

<sup>497</sup> where  $S^* = 1/\mathcal{R}_0$  represents the equilibrium proportion of susceptible individuals.  
<sup>498</sup> We vary the basic reproduction number  $\mathcal{R}_0$  between 1.1 to 6 and the average duration  
<sup>499</sup> of immunity  $1/\delta$  between 2 to 80 years, and compute these two quantities. In doing  
<sup>500</sup> so, we fix all other parameters:  $\mu = 1/80/\text{years}$  and  $\gamma = 365/7/\text{years}$ .

501 **Supplementary Text**

502 **Resilience of a stage-structured system.**

503 In Figure 2G–I, we use a more realistic, stage-structured model to illustrate how  
 504 transient phenomena can cause the system to slow down. Specifically, we use the  
 505 stage-structured RSV model proposed by [24], which assumes that subsequent rein-  
 506 fections cause an individual to become less susceptible and transmissible than previ-  
 507 ous infections. The model dynamics can be described as follows:

$$\frac{dM}{dt} = \mu - (\omega + \mu)M \quad (S1)$$

$$\frac{dS_0}{dt} = \omega M - (\lambda(t) + \mu)S_0 \quad (S2)$$

$$\frac{dI_1}{dt} = \lambda(t)S_0 - (\gamma_1 + \mu)I_1 \quad (S3)$$

$$\frac{dS_1}{dt} = \gamma_1 I_1 - (\sigma_1 \lambda(t) + \mu)S_1 \quad (S4)$$

$$\frac{dI_2}{dt} = \sigma_1 \lambda(t)S_1 - (\gamma_2 + \mu)I_2 \quad (S5)$$

$$\frac{dS_2}{dt} = \gamma_2 I_2 - (\sigma_2 \lambda(t) + \mu)S_2 \quad (S6)$$

$$\frac{dI_3}{dt} = \sigma_2 \lambda(t)S_2 - (\gamma_3 + \mu)I_3 \quad (S7)$$

$$\frac{dS_3}{dt} = \gamma_3 I_3 - (\sigma_3 \lambda(t) + \mu)S_3 + \gamma_4 I_4 \quad (S8)$$

$$\frac{dI_4}{dt} = \sigma_3 \lambda(t)S_3 - (\gamma_4 + \mu)I_4 \quad (S9)$$

(S10)

508 where  $M$  represents the proportion of individuals who are maternally immune;  $S_i$   
 509 represents the proportion of individuals who are susceptible after  $i$  prior infections;  $I_i$   
 510 represents the proportion of individuals who are currently (re)-infected with their  $i$ -th  
 511 infection;  $\mu$  represents the birth and death rates;  $1/\omega$  represents the mean duration  
 512 of maternal immunity;  $1/\gamma_i$  represents the mean duration of infection;  $\lambda(t)$  represents  
 513 the force of infection; and  $\sigma_i$  represents the reduction in susceptibility for reinfection.  
 514 The force of infection is modeled using a sinusoidal function:

$$\beta(t) = b_1(1 + \theta \cos(2\pi(t - \phi)))\alpha(t) \quad (S11)$$

$$\lambda(t) = \beta(I_1 + \rho_1 I_2 + \rho_2(I_3 + I_4)), \quad (S12)$$

515 where  $b_1$  represents the baseline transmission rate;  $\theta$  represents the seasonal ampli-  
 516 tude;  $\phi$  represents the seasonal offset term;  $\alpha(t)$  represents the intervention effect;  
 517 and  $\rho_i$  represents the impact of immunity on transmission reduction. We use the

518 following parameters to simulate the impact of interventions on epidemic dynam-  
 519 ics [24]:  $b_1 = 9 \times (365/10 + 1/80)/\text{years}$ ,  $\theta = 0.2$ ,  $\phi = -0.1$ ,  $\omega = 365/112/\text{years}$ ,  
 520  $\gamma_1 = 365/10/\text{years}$ ,  $\gamma_2 = 365/7/\text{years}$ ,  $\gamma_3 = 365/5/\text{years}$ ,  $\sigma_1 = 0.76$ ,  $\sigma_2 = 0.6$ ,  
 521  $\sigma_3 = 0.4$ ,  $\rho_1 = 0.75$ ,  $\rho_2 = 0.51$ , and  $\mu = 1/80/\text{years}$ . We assume a 50% transmission  
 522 reduction for 6 months from 2020:

$$\alpha(t) = \begin{cases} 0.5 & 2020 \leq t < 2020.5 \\ 1 & \text{otherwise} \end{cases} \quad (\text{S13})$$

523 The model is simulated from 1900 to 2030 using the following initial conditions:  
 524  $M = 0$ ,  $S_0 = 1/\mathcal{R}_0 - I_1$ ,  $I_1 = 1 \times 10^{-6}$ ,  $S_1 = 1 - 1/\mathcal{R}_0$ ,  $I_2 = 0$ ,  $S_2 = 0$ ,  $I_3 = 0$ ,  
 525  $S_3 = 0$ , and  $I_4 = 0$ . For the phase plane analysis (Figure 2H) and distance analysis  
 526 (Figure 2I), we rely on the average susceptibility,

$$\bar{S} = S_0 + \sigma_1 S_1 + \sigma_2 S_2 + \sigma_3 S_3, \quad (\text{S14})$$

527 and total prevalence,

$$I_{\text{total}} = I_1 + I_2 + I_3 + I_4. \quad (\text{S15})$$

528 These quantities are used to compute the normalized distance from the attractor, as  
 529 described in the main text.

## 530 Resilience of a multistrain system.

531 We use a simple two-strain model to show that a multistrain host-pathogen system  
 532 that is coupled through cross immunity can be described by a single resilience value.  
 533 The model dynamics can be described as follows [22]:

$$\frac{dS}{dt} = \mu - \mu S - (\lambda_1 + \lambda_2)S + \rho_1 R_1 + \rho_2 R_2 \quad (\text{S16})$$

$$\frac{dI_1}{dt} = \lambda_1 S - (\gamma_1 + \mu)I_1 \quad (\text{S17})$$

$$\frac{dI_2}{dt} = \lambda_2 S - (\gamma_2 + \mu)I_2 \quad (\text{S18})$$

$$\frac{dR_1}{dt} = \gamma_1 I_1 - \lambda_2 \epsilon_{21} R_1 - \rho_1 R_1 + \rho_2 R - \mu R_1 \quad (\text{S19})$$

$$\frac{dR_2}{dt} = \gamma_2 I_2 - \lambda_1 \epsilon_{12} R_2 - \rho_2 R_2 + \rho_1 R - \mu R_2 \quad (\text{S20})$$

$$\frac{dJ_1}{dt} = \lambda_1 \epsilon_{12} R_2 - (\gamma_1 + \mu) J_1 \quad (\text{S21})$$

$$\frac{dJ_2}{dt} = \lambda_2 \epsilon_{21} R_1 - (\gamma_2 + \mu) J_2 \quad (\text{S22})$$

$$\frac{dR}{dt} = \gamma_1 J_1 + \gamma_2 J_2 - \rho_1 R - \rho_2 R - \mu R \quad (\text{S23})$$

534 where  $S$  represents the proportion of individuals who are fully susceptible to infections  
 535 by both strains;  $I_1$  represents the proportion of individuals who are infected with strain 1 without prior immunity;  $I_2$  represents the proportion of individuals who are infected with strain 2 without prior immunity;  $R_1$  represents the proportion of individuals who are fully immune against strain 1 and partially susceptible to reinfection by strain 2;  $R_2$  represents the proportion of individuals who are fully immune against strain 2 and partially susceptible to reinfection by strain 1;  $J_1$  represents the proportion of individuals who are infected with strain 1 with prior immunity against strain 2;  $J_2$  represents the proportion of individuals who are infected with strain 2 with prior immunity against strain 1;  $R$  represents the proportion of individuals who are immune to infections from both strains;  $\mu$  represents the birth/death rate;  $\lambda_1$  and  $\lambda_2$  represent the force of infection from strains 1 and 2, respectively;  $\rho_1$  and  $\rho_2$  represent the waning immunity rate;  $\gamma_1$  and  $\gamma_2$  represent the recovery rate;  $\epsilon_{12}$  and  $\epsilon_{21}$  represent the susceptibility to reinfection with strains 2 and 1, respectively, given prior immunity from infection with strains 1 and 2, respectively. The force of infection is modeled as follows:

$$\beta_1 = b_1(1 + \theta_1 \sin(2\pi(t - \phi_1)))\alpha(t) \quad (\text{S24})$$

$$\beta_2 = b_2(1 + \theta_2 \sin(2\pi(t - \phi_2)))\alpha(t) \quad (\text{S25})$$

$$\lambda_1 = \beta_1(I_1 + J_1) \quad (\text{S26})$$

$$\lambda_2 = \beta_2(I_2 + J_2) \quad (\text{S27})$$

550 In Supplementary Figures S2–S4, we assume the following parameters:  $b_1 = 2 \times$   
 551  $52/\text{years}$ ,  $b_2 = 4 \times 52/\text{years}$ ,  $\phi_1 = \phi_2 = 0$ ,  $\epsilon_{12} = 0.9$ ,  $\epsilon_{21} = 0.5$ ,  $\gamma_1 = \gamma_2 = 52/\text{years}$ ,  
 552  $\rho_1 = \rho_2 = 1/\text{years}$ , and  $\mu = 1/70/\text{years}$ . For all simulations, we assume a 50%  
 553 transmission reduction for 6 months from 2020:

$$\alpha(t) = \begin{cases} 0.5 & 2020 \leq t < 2020.5 \\ 1 & \text{otherwise} \end{cases} \quad (\text{S28})$$

554 The seasonal amplitude  $\theta$  is varied from 0 to 0.4. All simulations are ran from 1900  
 555 to 2030 from the following initial conditions:  $S(0) = 1 - 2 \times 10^{-6}$ ,  $I_1(0) = 1 \times 10^{-6}$ ,  
 556  $I_2(0) = 1 \times 10^{-6}$ ,  $R_1(0) = 0$ ,  $R_2(0) = 0$ ,  $J_1(0) = 0$ ,  $J_2(0) = 0$ , and  $R(0) = 0$ .

557 For this, we consider three different scenarios for measuring pathogen resilience:  
 558 (1) we only have information about strain 1, (2) we only have information about  
 559 strain 2, and (3) we are unable to distinguish the differences between strains. In  
 560 the first two scenarios (see panels A–C for strain 1 and panels D–F for strain 2), we  
 561 consider the dynamics of average susceptibility for each strain and total prevalence:

$$\bar{S}_1 = S + \epsilon_{12}R_2 \quad (\text{S29})$$

$$\hat{I}_1 = I_1 + J_1 \quad (\text{S30})$$

$$\bar{S}_2 = S + \epsilon_{21}R_1 \quad (\text{S31})$$

$$\hat{I}_2 = I_2 + J_2 \quad (\text{S32})$$

562 In the third scenario (panels G–I), we consider the dynamics of total susceptible and  
563 infected population:

$$\hat{S} = S + R_2 + R_1 \quad (\text{S33})$$

$$\hat{I} = I_1 + J_1 + I_2 + J_2 \quad (\text{S34})$$

$$(\text{S35})$$

564 These quantities are used to compute the normalized distance from the attractor, as  
565 described in the main text.

## 566 Estimating intrinsic resilience using mechanistic model

567 We test whether we can reliably estimate the intrinsic resilience of a system by fitting  
568 a mechanistic model. Specifically, we simulate case time series from stochastic SIRS  
569 and two-strain models and fit a simple, deterministic SIRS model using a Bayesian  
570 framework.

571 First, we describe the simulation set up. The stochastic SIRS model can be  
572 written as follows:

$$\beta(t) = \mathcal{R}_0 \left( 1 + \theta \cos \left( \frac{2\pi t}{364} \right) \right) \alpha(t)(1 - \exp(-\gamma)) \quad (\text{S36})$$

$$\text{FOI}(t) = \beta(t)I(t - \Delta t)/N \quad (\text{S37})$$

$$B(t) \sim \text{Poisson}(\mu N) \quad (\text{S38})$$

$$\Delta S(t) \sim \text{Binom}(S(t - \Delta t), 1 - \exp(-(\text{FOI}(t) + \mu)\Delta t)) \quad (\text{S39})$$

$$N_{SI}(t) \sim \text{Binom}\left(\Delta S(t), \frac{\text{FOI}(t)}{\text{FOI}(t) + \mu}\right) \quad (\text{S40})$$

$$\Delta I(t) \sim \text{Binom}(I(t - \Delta t), 1 - \exp(-(\gamma + \mu)\Delta t)) \quad (\text{S41})$$

$$N_{IR}(t) \sim \text{Binom}\left(\Delta I(t), \frac{\gamma}{\gamma + \mu}\right) \quad (\text{S42})$$

$$\Delta R(t) \sim \text{Binom}(R(t - \Delta t), 1 - \exp(-(\delta + \mu)\Delta t)) \quad (\text{S43})$$

$$N_{RS}(t) \sim \text{Binom}\left(\Delta R(t), \frac{\delta}{\delta + \mu}\right) \quad (\text{S44})$$

$$S(t) = S(t - \Delta t) + N_{RS}(t) + B(t) - \Delta S(t) \quad (\text{S45})$$

$$I(t) = I(t - \Delta t) + N_{SI}(t) - \Delta I(t) \quad (\text{S46})$$

$$R(t) = R(t - \Delta t) + N_{IR}(t) - \Delta R(t) \quad (\text{S47})$$

573 where FOI represent the force of infection;  $N_{ij}$  represent the number of individuals  
574 moving from compartment  $i$  to  $j$  on a given day; and  $B(t)$  represents the number  
575 of new births. We simulate the model on a daily scale—assuming 364 days in a  
576 year so that it can be evenly grouped into 52 weeks—with the following parameters:  
577  $\mathcal{R}_0 = 3$ ,  $\theta = 0.1$ ,  $\gamma = 1/7/\text{days}$ ,  $\delta = 1/(364 \times 2)/\text{days}$ ,  $\mu = 1/(364 \times 50)/\text{days}$ , and

578  $N = 1 \times 10^8$ . The model is simulated from 1900 to 2030 assuming  $S(0) = N/3$ ,  
 579  $I(0) = 100$ , and  $R(0) = N - S(0) - I(0)$ . The observed incidence from the model is  
 580 then simulated as follows:

$$C(t) = \text{Beta} - \text{Binom}(N_{SI}(t), \rho, k), \quad (\text{S48})$$

581 where  $\rho$  represents the reporting probability and  $k$  represents the overdispersion pa-  
 582 rameter of beta-binomial distribution. We assume  $\rho = 0.002$  (i.e., 0.2% probability)  
 583 and  $k = 1000$ .

584 The stochastic two-strain model can be written as follows:

$$\beta_1(t) = b_1 \left( 1 + \theta_1 \cos \left( \frac{2\pi(t - \phi_1)}{364} \right) \right) \alpha(t) \quad (\text{S49})$$

$$\beta_2(t) = b_2 \left( 1 + \theta_2 \cos \left( \frac{2\pi(t - \phi_2)}{364} \right) \right) \alpha(t) \quad (\text{S50})$$

$$\text{FOI}_1(t) = \beta_1(t)(I_1(t - \Delta t) + J_1(t - \Delta t))/N \quad (\text{S51})$$

$$\text{FOI}_2(t) = \beta_2(t)(I_2(t - \Delta t) + J_2(t - \Delta t))/N \quad (\text{S52})$$

$$B(t) \sim \text{Poisson}(\mu N) \quad (\text{S53})$$

$$\Delta S(t) \sim \text{Binom}(S(t - \Delta t), 1 - \exp(-(\text{FOI}_1(t) + \text{FOI}_2(t) + \mu)\Delta t)) \quad (\text{S54})$$

$$N_{SI_1}(t) \sim \text{Binom}\left(\Delta S(t), \frac{\text{FOI}_1(t)}{\text{FOI}_1(t) + \text{FOI}_2(t) + \mu}\right) \quad (\text{S55})$$

$$N_{SI_2}(t) \sim \text{Binom}\left(\Delta S(t), \frac{\text{FOI}_2(t)}{\text{FOI}_1(t) + \text{FOI}_2(t) + \mu}\right) \quad (\text{S56})$$

$$\Delta I_1(t) \sim \text{Binom}(I_1(t - \Delta t), 1 - \exp(-(\gamma_1 + \mu)\Delta t)) \quad (\text{S57})$$

$$N_{I_1 R_1}(t) \sim \text{Binom}\left(\Delta I_1(t), \frac{\gamma_1}{\gamma_1 + \mu}\right) \quad (\text{S58})$$

$$\Delta I_2(t) \sim \text{Binom}(I_2(t - \Delta t), 1 - \exp(-(\gamma_2 + \mu)\Delta t)) \quad (\text{S59})$$

$$N_{I_2 R_2}(t) \sim \text{Binom}\left(\Delta I_2(t), \frac{\gamma_2}{\gamma_2 + \mu}\right) \quad (\text{S60})$$

$$\Delta R_1(t) \sim \text{Binom}(R_1(t - \Delta t), 1 - \exp(-(\epsilon_{21}\text{FOI}_2(t) + \rho_1 + \mu)\Delta t)) \quad (\text{S61})$$

$$N_{R_1 S}(t) \sim \text{Binom}\left(\Delta R_1(t), \frac{\rho_1}{\epsilon_{21}\text{FOI}_2(t) + \rho_1 + \mu}\right) \quad (\text{S62})$$

$$N_{R_1 J_2}(t) \sim \text{Binom}\left(\Delta R_1(t), \frac{\epsilon_{21}\text{FOI}_2(t)}{\epsilon_{21}\text{FOI}_2(t) + \rho_1 + \mu}\right) \quad (\text{S63})$$

$$\Delta R_2(t) \sim \text{Binom}(R_2(t - \Delta t), 1 - \exp(-(\epsilon_{12}\text{FOI}_1(t) + \rho_2 + \mu)\Delta t)) \quad (\text{S64})$$

$$N_{R_2 S}(t) \sim \text{Binom}\left(\Delta R_2(t), \frac{\rho_2}{\epsilon_{12}\text{FOI}_1(t) + \rho_2 + \mu}\right) \quad (\text{S65})$$

$$N_{R_2 J_1}(t) \sim \text{Binom}\left(\Delta R_2(t), \frac{\epsilon_{12}\text{FOI}_1(t)}{\epsilon_{12}\text{FOI}_1(t) + \rho_2 + \mu}\right) \quad (\text{S66})$$

$$\Delta J_1(t) \sim \text{Binom}(J_1(t - \Delta t), 1 - \exp(-(\gamma_1 + \mu)\Delta t)) \quad (\text{S67})$$

$$N_{J_1R}(t) \sim \text{Binom}\left(\Delta J_1(t), \frac{\gamma_1}{\gamma_1 + \mu}\right) \quad (\text{S68})$$

$$\Delta J_2(t) \sim \text{Binom}(J_2(t - \Delta t), 1 - \exp(-(\gamma_2 + \mu)\Delta t)) \quad (\text{S69})$$

$$N_{J_2R}(t) \sim \text{Binom}\left(\Delta J_2(t), \frac{\gamma_2}{\gamma_2 + \mu}\right) \quad (\text{S70})$$

$$\Delta R(t) \sim \text{Binom}(R(t - \Delta t), 1 - \exp(-(\rho_1 + \rho_2 + \mu)\Delta t)) \quad (\text{S71})$$

$$N_{RR_1}(t) \sim \text{Binom}\left(\Delta R(t), \frac{\rho_1}{\rho_1 + \rho_2 + \mu}\right) \quad (\text{S72})$$

$$N_{RR_2}(t) \sim \text{Binom}\left(\Delta R(t), \frac{\rho_2}{\rho_1 + \rho_2 + \mu}\right) \quad (\text{S73})$$

$$S(t) = S(t - \Delta t) - \Delta S(t) + B(t) + N_{R_1S}(t) + N_{R_2S}(t) \quad (\text{S74})$$

$$I_1(t) = I_1(t - \Delta t) - \Delta I_1(t) + N_{SI_1}(t) \quad (\text{S75})$$

$$I_2(t) = I_2(t - \Delta t) - \Delta I_2(t) + N_{SI_2}(t) \quad (\text{S76})$$

$$R_1(t) = R_1(t - \Delta t) - \Delta R_1(t) + N_{I_1R_1}(t) + N_{RR_1}(t) \quad (\text{S77})$$

$$R_2(t) = R_2(t - \Delta t) - \Delta R_2(t) + N_{I_2R_2}(t) + N_{RR_2}(t) \quad (\text{S78})$$

$$J_1(t) = J_1(t - \Delta t) - \Delta J_1(t) + N_{R_2J_1}(t) \quad (\text{S79})$$

$$J_2(t) = J_2(t - \Delta t) - \Delta J_2(t) + N_{R_1J_2}(t) \quad (\text{S80})$$

$$R(t) = R(t - \Delta t) - \Delta R(t) + N_{J_1R}(t) + N_{J_2R}(t) \quad (\text{S81})$$

585 We simulate the model on a daily scale with previously estimated parameters for the  
 586 RSV-HMPV interaction [22]:  $b_1 = 1.7/\text{weeks}$ ,  $b_2 = 1.95/\text{weeks}$ ,  $\theta_1 = 0.4$ ,  $\theta_2 = 0.3$ ,  
 587  $\phi_1 = 0.005 \times 7/364$ ,  $\phi_2 = 4.99 \times 7/364$ ,  $\epsilon_{12} = 0.92$ ,  $\epsilon_{21} = 0.45$ ,  $\gamma_1 = 1/10/\text{days}$ ,  
 588  $\gamma_2 = 1/10/\text{days}$ ,  $\rho_1 = 1/364/\text{days}$ ,  $\rho_2 = 1/364/\text{days}$ ,  $\mu = 1/(70 \times 364)/\text{days}$ , and  
 589  $N = 1 \times 10^8$ . The model is simulated from 1900 to 2030 assuming  $S(0) = N - 200$ ,  
 590  $I_1(0) = 100$ ,  $I_2(0) = 100$ ,  $R_1(0) = 0$ ,  $R_2(0) = 0$ ,  $J_1(0) = 0$ ,  $J_2(0) = 0$ , and  $R(0) = 0$ .  
 591 The observed incidence for each strain is then simulated as follows:

$$C_1(t) = \text{Beta} - \text{Binom}(N_{SI_1}(t) + N_{R_2J_1}, \rho, k), \quad (\text{S82})$$

$$C_2(t) = \text{Beta} - \text{Binom}(N_{SI_2}(t) + N_{R_1J_2}, \rho, k), \quad (\text{S83})$$

592 where  $\rho$  represents the reporting probability and  $k$  represents the overdispersion pa-  
 593 rameter of beta-binomial distribution. We assume  $\rho = 0.002$  (i.e., 0.2% probability)  
 594 and  $k = 500$ . We also consider the total incidence:  $C_{\text{total}}(t) = C_1(t) + C_2(t)$ .

595 For both models, we consider a more realistic challenges in intervention effects  
 596  $\alpha(t)$  to challenge our ability to estimate the intervention effects. Thus, we assume  
 597 a 40% transmission reduction for 3 months from March 2020, followed by a 10%  
 598 transmission reduction for 6 months, 20% transmission reduction for 3 months, and

599 a final return to normal levels:

$$\alpha(t) = \begin{cases} 1 & t < 2020.25 \\ 0.6 & 2020.25 \leq t < 2020.5 \\ 0.9 & 2020.5 \leq t < 2021 \\ 0.8 & 2021 \leq t < 2021.25 \\ 1 & 2021.25 \leq t \end{cases}. \quad (\text{S84})$$

600 For all simulations, we truncate the time series from the beginning of 2014 to the  
601 end of 2023 and aggregate them into weekly cases.

602 To infer intrinsic resilience from time series, we fit a simple discrete time, deter-  
603 ministic SIRS model [4]:

$$\Delta t = 1 \text{ week} \quad (\text{S85})$$

$$\text{FOI}(t) = \beta(t)(I(t - \Delta t) + \omega)/N \quad (\text{S86})$$

$$\Delta S(t) = [1 - \exp(-(\text{FOI}(t) + \mu)\Delta t)] S(t - \Delta t) \quad (\text{S87})$$

$$N_{SI}(t) = \frac{\text{FOI}(t)\Delta S(t)}{\text{FOI}(t) + \mu} \quad (\text{S88})$$

$$\Delta I(t) = [1 - \exp(-(\gamma + \mu)\Delta t)] I(t - \Delta t) \quad (\text{S89})$$

$$N_{IR}(t) = \frac{\gamma \Delta I(t)}{\gamma + \mu} \quad (\text{S90})$$

$$\Delta R(t) = [1 - \exp(-(\nu + \mu)\Delta t)] R(t - \Delta t) \quad (\text{S91})$$

$$N_{RS}(t) = \frac{\nu \Delta R(t)}{\nu + \mu} \quad (\text{S92})$$

$$S(t) = S(t - \Delta t) + \mu S - \Delta S(t) + N_{RS}(t) \quad (\text{S93})$$

$$I(t) = I(t - \Delta t) - \Delta I(t) + N_{SI}(t) \quad (\text{S94})$$

$$R(t) = R(t - \Delta t) - \Delta R(t) + N_{IR}(t) \quad (\text{S95})$$

604 where we include an extra term  $\omega$  to account for external infections. Although actual  
605 simulations do not include any external infections, we found that including this term  
606 generally helped with model convergence in previous analyses [4]. The transmission  
607 rate is divided into a seasonal term  $\beta_{\text{seas}}(t)$  (repeated every year) and intervention  
608 term  $\alpha(t)$ , which are estimated jointly:

$$\beta(t) = \beta_{\text{seas}}(t)\alpha(t), \quad (\text{S96})$$

609 where  $\alpha < 1$  corresponds to reduction in transmission due to intervention effects. To  
610 constrain the smoothness of  $\beta_{\text{seas}}(t)$ , we impose cyclic, random-walk priors:

$$\beta_{\text{seas}}(t) \sim \text{Normal}(\beta_{\text{seas}}(t - 1), \sigma) \quad t = 2 \dots 52 \quad (\text{S97})$$

$$\beta_{\text{seas}}(1) \sim \text{Normal}(\beta_{\text{seas}}(52), \sigma) \quad (\text{S98})$$

611 [SWP: I noticed that I forgot to put a prior on  $\sigma$  so need to re-do this but won't  
 612 change the results.] We fix  $\alpha(t) = 1$  for all  $t < 2020$  and estimate  $\alpha$  assuming a  
 613 normal prior:

$$\alpha \sim \text{Normal}(1, 0.25). \quad (\text{S99})$$

614 We assume weakly informative priors on  $\omega$  and  $\tau$ :

$$\omega \sim \text{Normal}(0, 200) \tau \sim \text{Normal}(104, 26) \quad (\text{S100})$$

615 We assume that the true birth/death rates, population sizes, and recovery rates are  
 616 known. We note, however, that assuming  $\gamma = 1/\text{week}$  actually correspond to a  
 617 mean infectious period of 1.6 weeks, which is much longer than the true value; this  
 618 approximation allows us to test whether we can still robustly estimate the intrinsic  
 619 resilience given parameters mis-specification. Initial conditions are estimated with  
 620 following priors:

$$S(0) = Ns(0) \quad (\text{S101})$$

$$I(0) = Ni(0) \quad (\text{S102})$$

$$s(0) \sim \text{Uniform}(0, 1) \quad (\text{S103})$$

$$i(0) \sim \text{Half-Normal}(0, 0.001) \quad (\text{S104})$$

621 Finally, the Observation model is specified as follows:

$$\text{Cases}(t) \sim \text{Negative-Binomial}(\rho N_{SI}(t), \phi) \quad (\text{S105})$$

$$\rho \sim \text{Half-Normal}(0, 0.02) \quad (\text{S106})$$

$$\phi \sim \text{Half-Normal}(0, 10) \quad (\text{S107})$$

622 where  $\rho$  represents the reporting probability and  $\phi$  represents the negative binomial  
 623 overdispersion parameter.

624 The model is fitted to four separate time series: (1) incidence time series from  
 625 the SIRS model, (2) incidence time series for strain 1 from the two-strain model,  
 626 (3) incidence time series for strain 2 from the two-strain model, and (4) combined  
 627 incidence time series for strains 1 and 2 from the two-strain model. The model was  
 628 fitted using rstan [29, 30]. The resulting posterior distribution was used to calculate  
 629 the intrinsic resilience of the seasonally unforced system with the same parameters;  
 630 eigenvalues of the discrete-time SIR model were computed by numerically finding  
 631 the equilibrium and calculating the Jacobian matrix.

## 632 **Validations for window-selection criteria**

633 We use stochastic SIRS simulations to validate the window-selection criteria that we  
 634 use for the linear regression for estimating empirical resilience. For each simulation,  
 635 we begin by generating a random intervention  $\alpha(t)$  from random set of parameters.  
 636 First, we draw the duration of intervention  $\tau_{\text{np}}^*$  from a uniform distribution between

637 0.5 and 3.5 years. Then, we draw independent normal variables  $z_i$  of length  $\lfloor 364\tau_{\text{npi}} \rfloor$   
 638 with a standard deviation of 0.02 and take a reverse cumulative sum to obtain a  
 639 realistic shape for the intervention:

$$x_n = 1 + \sum_{i=n}^{\lfloor 364\tau_{\text{npi}} \rfloor} z_i, \quad n = 1, \dots, \lfloor 364\tau_{\text{npi}} \rfloor. \quad (\text{S108})$$

640 We repeat this random generation process until less than 10% of  $x_n$  exceeds 1. Then,  
 641 we set any values that are above 1 or below 0 as 1 and 0, respectively. Then, we  
 642 randomly draw the minimum transmission during intervention  $\alpha_{\min}$  from a uniform  
 643 distribution between 0.5 and 0.7 and scale  $x_n$  to have a minimum of  $\alpha_{\min}$ :

$$x_{\text{scale},n} = \alpha_{\min} + (1 - \alpha_{\min}) \times \frac{x_n - \min x_n}{1 - \min x_n}. \quad (\text{S109})$$

644 This allows us to simulate a realistically shaped interventions:

$$\alpha(t) = \begin{cases} 1 & t < 2020 \\ x_{\text{scale},364(t-2020)} & 2020 \leq t < 2020 + \tau_{\text{npi}} \\ 1 & \tau_{\text{npi}} \leq t \end{cases}. \quad (\text{S110})$$

645 Given this intervention function, we draw  $\mathcal{R}_0$  from a uniform distribution between 1.5  
 646 and 3 and the mean duration of immunity  $1/\delta$  from a uniform distribution between  
 647 0.5 and 2. Then, we simulate the stochastic SIRS model from  $S(0) = 10^8/\mathcal{R}_0$  and  
 648  $I(0) = 100$  from 1990 to 2025 and truncate the time series to 2014–2025; if the  
 649 epidemic becomes extinct before the end of simulation, we discard that simulation  
 650 and start over from the intervention generation step. We then apply the window  
 651 selection criteria described in the main text to compute the empirical resilience and  
 652 compare it against the intrinsic resilience of the seasonally unforced system. We also  
 653 compare this with the naive approach that uses the entire distance-from-attractor  
 654 time series, starting from the maximum distance. We repeat this procedure 500  
 655 times and quantify the correlation between empirical and intrinsic resilience estimates  
 656 across two approaches.

# Supplementary Figures

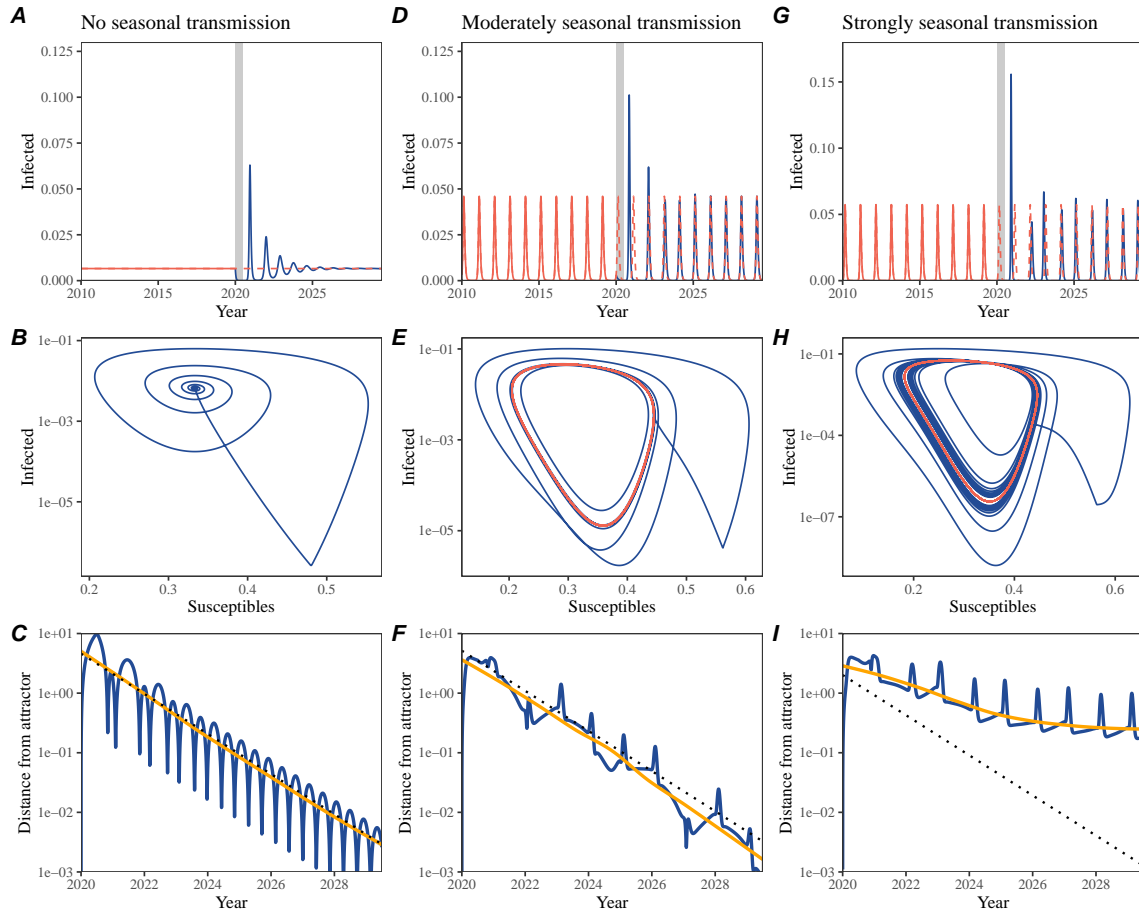


**Figure S1: Impact of seasonal transmission on pathogen resilience.** (A, D, G) Simulated epidemic trajectories using the SIRS model without seasonal forcing (A), with seasonal forcing of amplitude of 0.2 (D), and with seasonal forcing of amplitude of 0.2 (G). Red and blue solid lines represent epidemic dynamics before and after interventions are introduced, respectively. Red dashed lines represent counterfactual epidemic dynamics in the absence of interventions. Gray regions indicate the duration of interventions. (B, E, H) Phase plane representation of the corresponding model. Red and blue solid lines represent epidemic trajectories on an SI phase plane before and after interventions are introduced, respectively. (C, F, I) Changes in logged distance from attractor over time. Blue lines represent the logged distance from attractor. Orange lines represent the locally estimated scatterplot smoothing (LOESS) fits to the logged distance from attractor. Dotted lines are superimposed as a comparison to have the same slope as the intrinsic resilience of the seasonally unforced system.

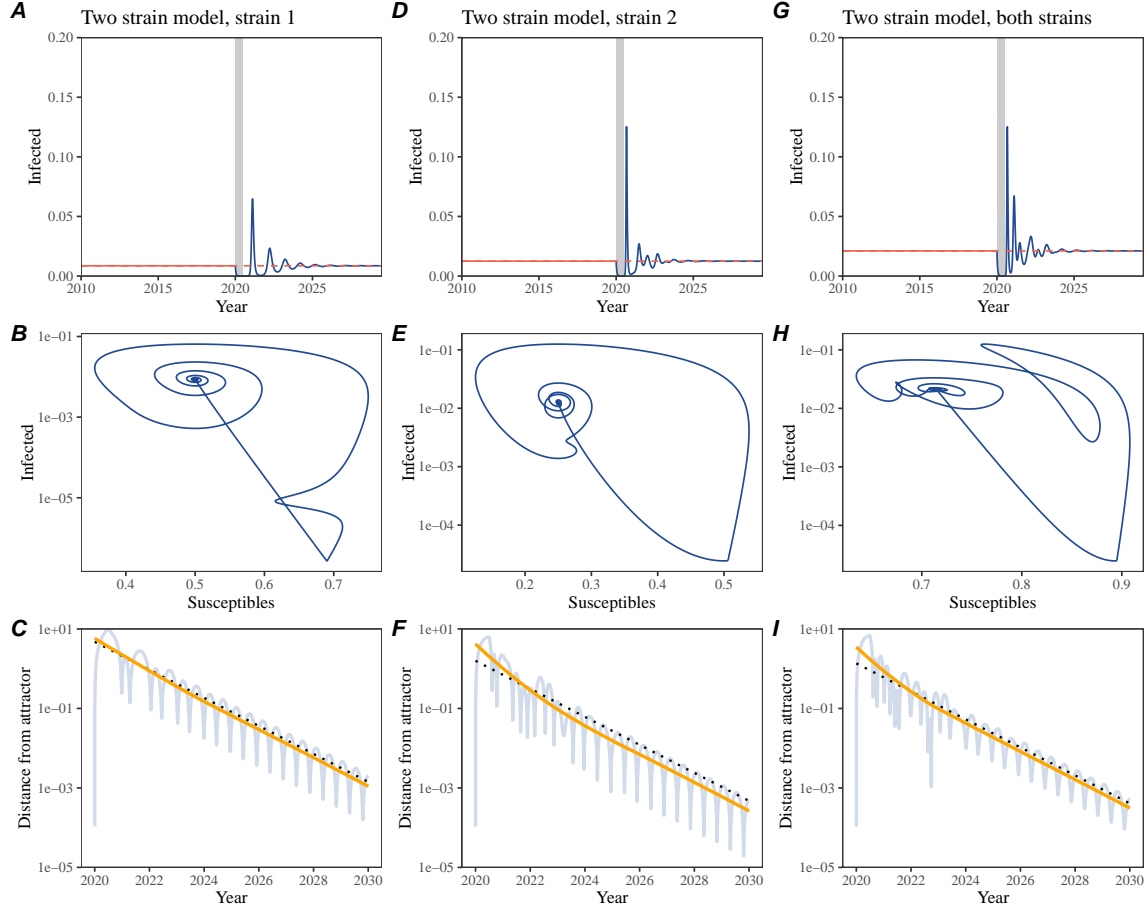


**Figure S2: Conceptual framework for measuring pathogen resilience following NPIs for a multi-strain system without seasonal forcing.** (A, D, G) Simulated epidemic trajectories using a multi-strain system without seasonal forcing. Red and blue solid lines represent epidemic dynamics before and after interventions are introduced, respectively. Red dashed lines represent counterfactual epidemic dynamics in the absence of interventions. Gray regions indicate the duration of interventions. (B, E, H) Phase plane representation of the corresponding model. Red and blue solid lines represent epidemic trajectories on an SI phase plane before and after interventions are introduced, respectively. (C, F, I) Changes in logged distance from attractor over time. Blue lines represent the logged distance from attractor. Orange lines represent the locally estimated scatterplot smoothing (LOESS) fits to the logged distance from attractor. Dotted lines are superimposed as a comparison to have the same slope as the intrinsic resilience of the seasonally unforced system.

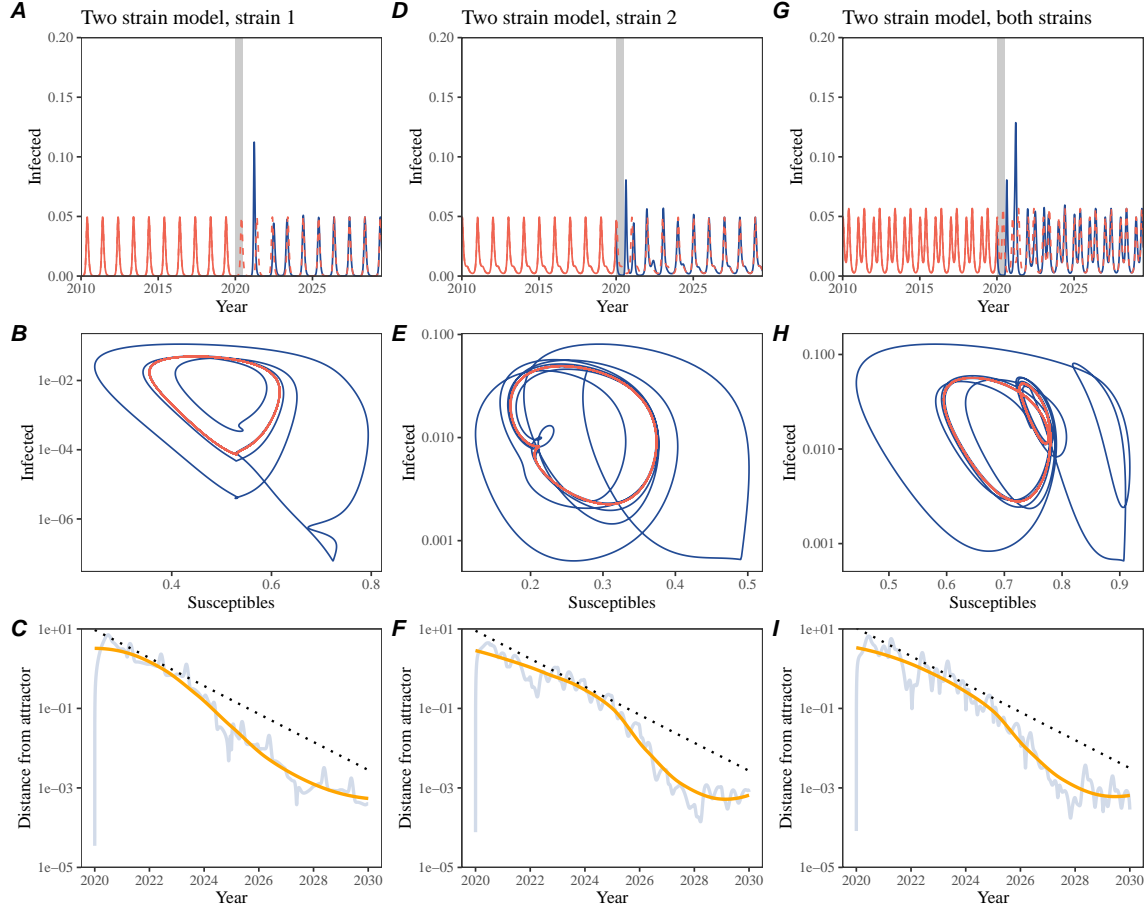


**Figure S3: Conceptual framework for measuring pathogen resilience following NPIs for a multi-strain system with seasonal forcing.** (A, D, G) Simulated epidemic trajectories using a multi-strain system with seasonal forcing (amplitude of 0.2). Red and blue solid lines represent epidemic dynamics before and after interventions are introduced, respectively. Red dashed lines represent counterfactual epidemic dynamics in the absence of interventions. Gray regions indicate the duration of interventions. (B, E, H) Phase plane representation of the corresponding model. Red and blue solid lines represent epidemic trajectories on an SI phase plane before and after interventions are introduced, respectively. (C, F, I) Changes in logged distance from attractor over time. Blue lines represent the logged distance from attractor. Orange lines represent the locally estimated scatterplot smoothing (LOESS) fits to the logged distance from attractor. Dotted lines are superimposed as a comparison to have the same slope as the intrinsic resilience of the seasonally unforced system.

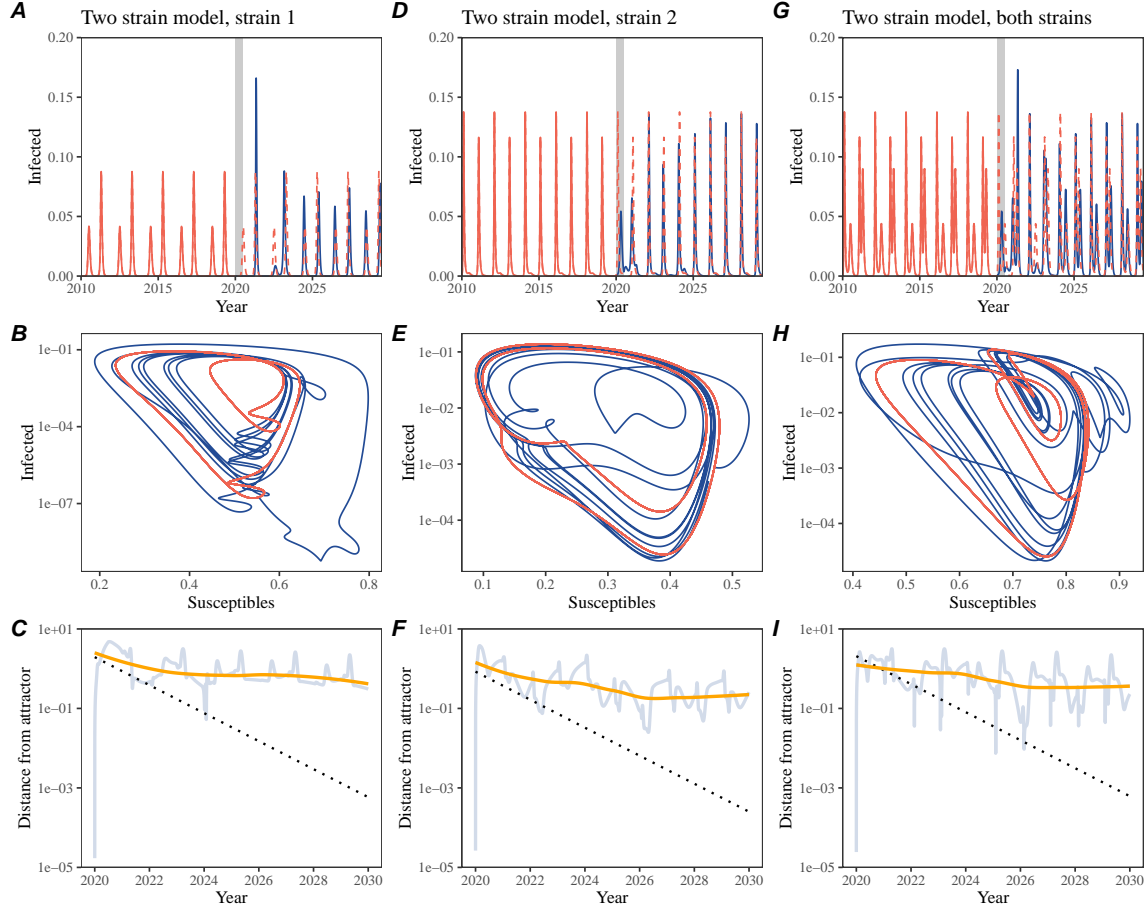


**Figure S4: Conceptual framework for measuring pathogen resilience following NPIs for a multi-strain system with strong seasonal forcing.** (A, D, G) Simulated epidemic trajectories using a multi-strain system with seasonal forcing (amplitude of 0.4). Red and blue solid lines represent epidemic dynamics before and after interventions are introduced, respectively. Red dashed lines represent counterfactual epidemic dynamics in the absence of interventions. Gray regions indicate the duration of interventions. (B, E, H) Phase plane representation of the corresponding model. Red and blue solid lines represent epidemic trajectories on an SI phase plane before and after interventions are introduced, respectively. (C, F, I) Changes in logged distance from attractor over time. Blue lines represent the logged distance from attractor. Orange lines represent the locally estimated scatterplot smoothing (LOESS) fits to the logged distance from attractor. Dotted lines are superimposed as a comparison to have the same slope as the intrinsic resilience of the seasonally unforced system.

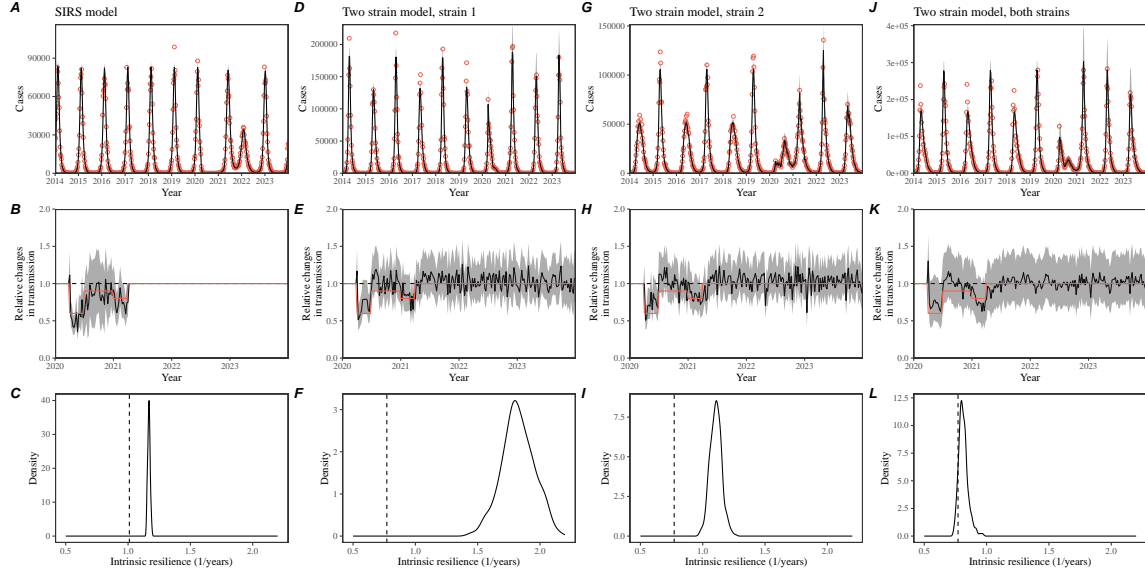


**Figure S5: Mechanistic model fits to simulated data and inferred intrinsic resilience.** (A, D, G, J) Simulated case time series from corresponding models (red) and SIRS model fits (black). (B, E, H, K) Assumed changes in transmission due to COVID-19 interventions (red) and estimated changes from the SIRS model (black). Solid lines and shaded regions represent fitted posterior median and 95% credible intervals. (C, F, I, L) True intrinsic resilience of the seasonally unforced system (vertical lines) and the posterior distribution of the inferred intrinsic resilience from the SIRS model (density plots).

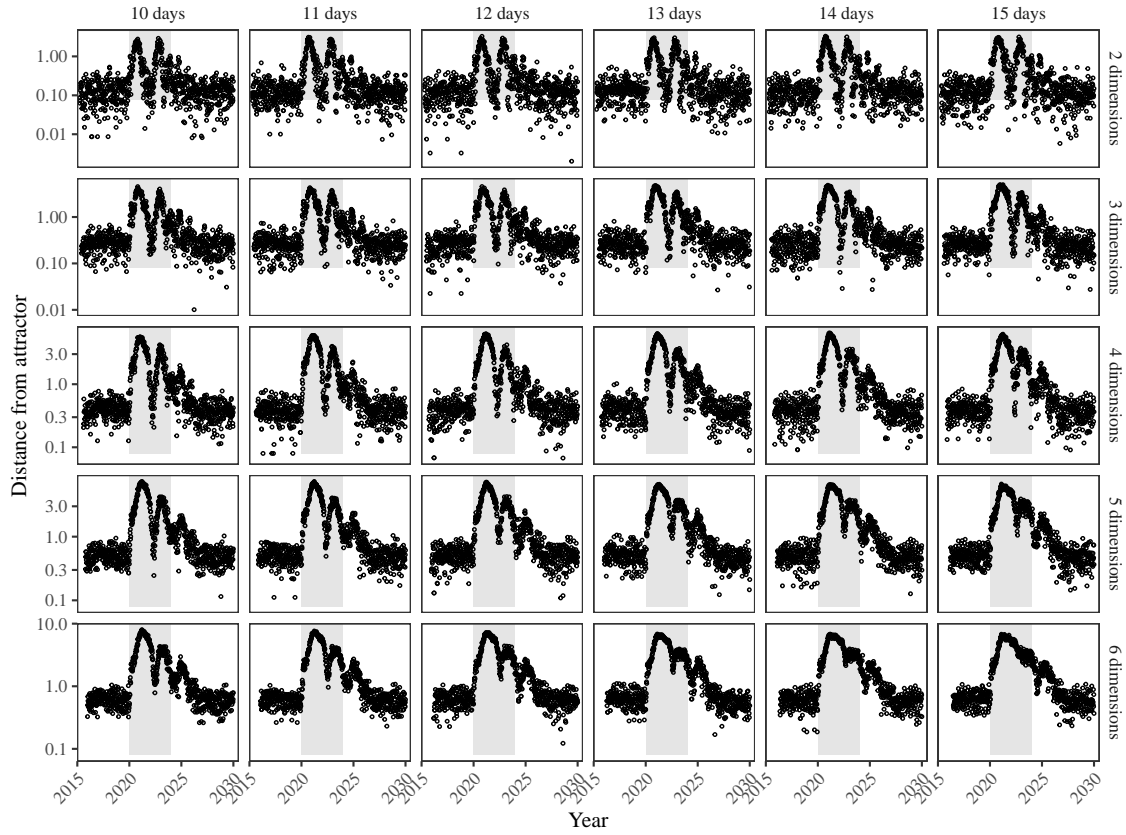


**Figure S6: Sensitivity of the distance from attractor to choices about embedding lags and dimensions.** Sensitivity analysis for the distance-from-attractor time series shown in Figure 3E in the main text by varying the embedding lag between 10–15 days and embedding dimensions between 2–6 dimensions.

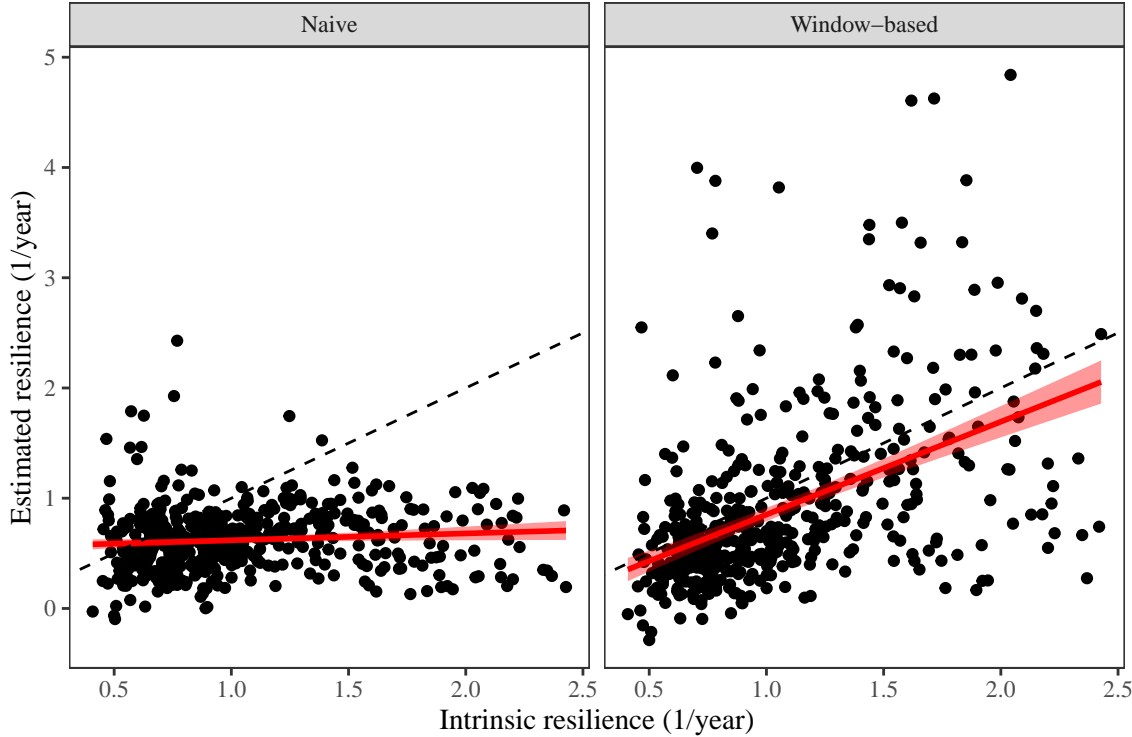


**Figure S7: Impact of fitting window selection on the estimation of empirical resilience.** We simulate 500 epidemics using stochastic SIRS model with randomly drawn parameters and randomly generated intervention impacts. For each simulation, we reconstruct the empirical attractor based on the approach outlined in Figure 3 and estimate the distance from attractor. The naive approach fits a linear regression on a log scale, starting from the maximum distance until the end of the time series. The window-based approach tries to select an appropriate window by smoothing the distance estimates and finding a time period when the smoothed time series crosses pre-determined threshold, relatively to the maximum distance; then, a linear regression is fitted by using the raw distance within this time period.

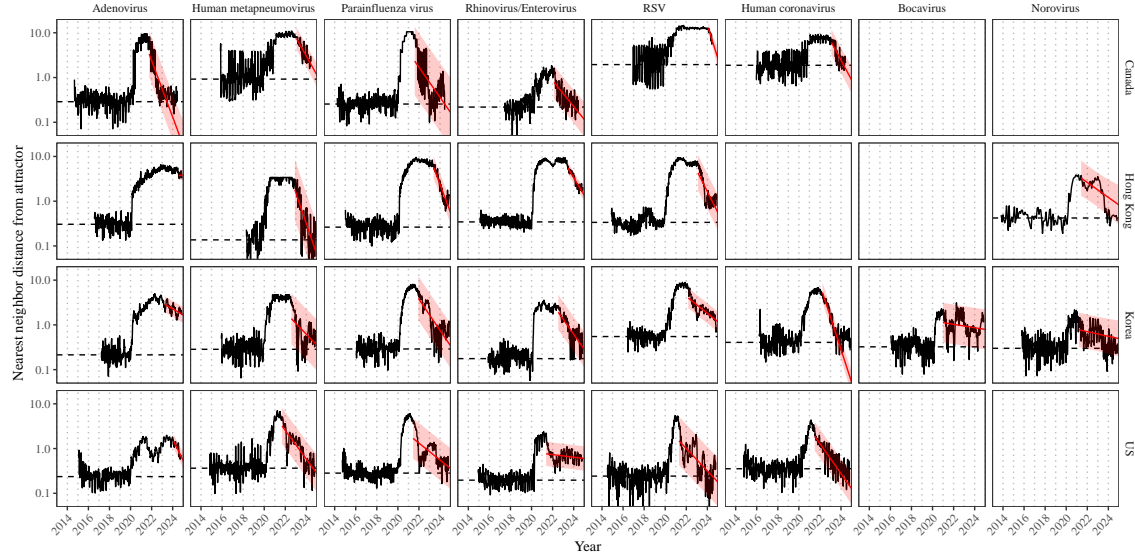


**Figure S8: Estimated time series of distance from attractor for each pathogen across Canada, Hong Kong, Korea, and the US.** Black lines represent the estimated distance from attractor. Red lines and shaded regions represent the linear regression fits and corresponding 95% confidence intervals. Dashed lines represent the average of the pre-pandemic nearest neighbor distances.

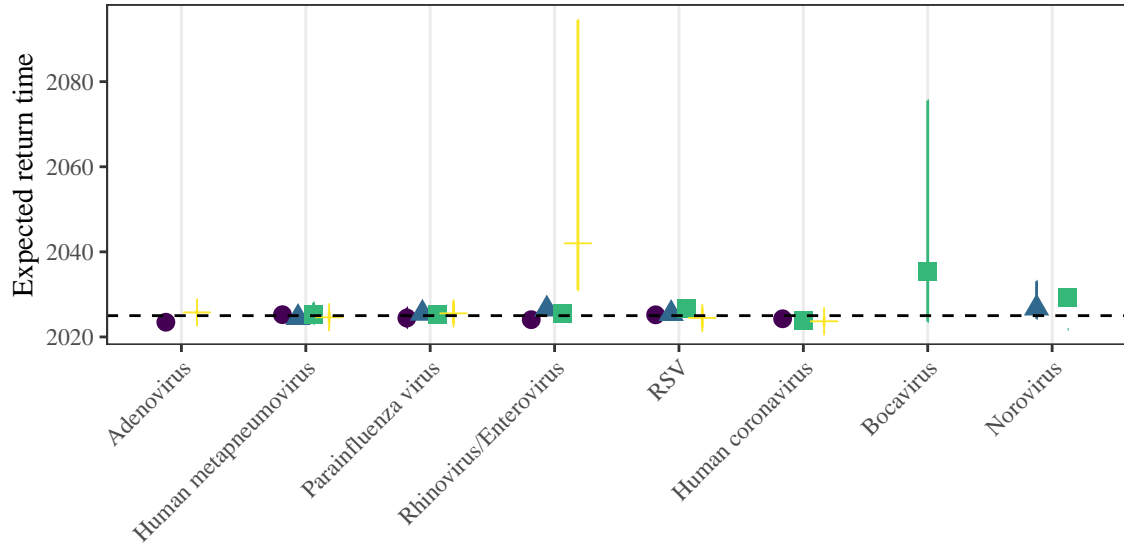
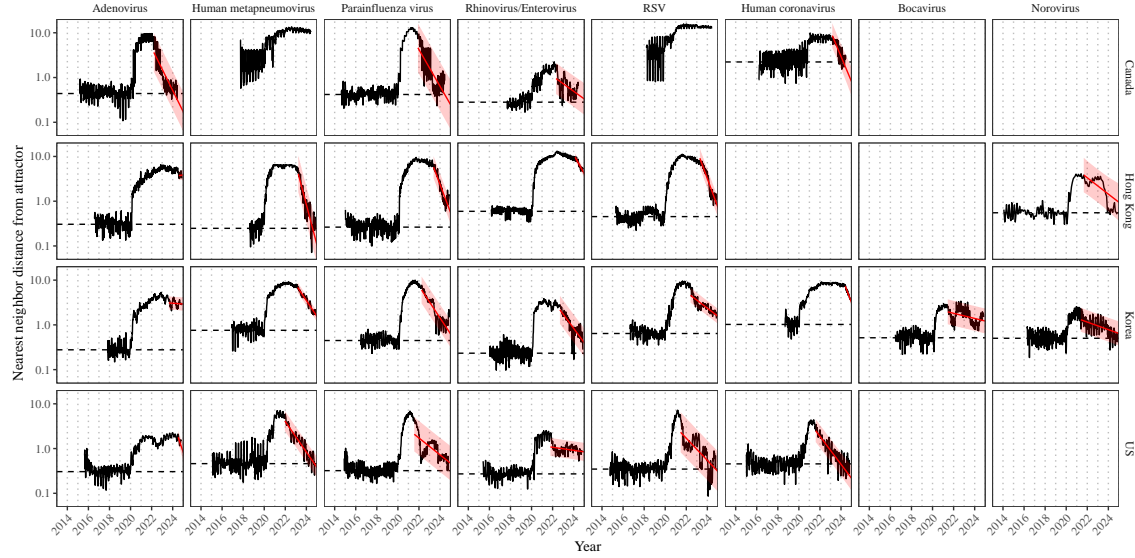
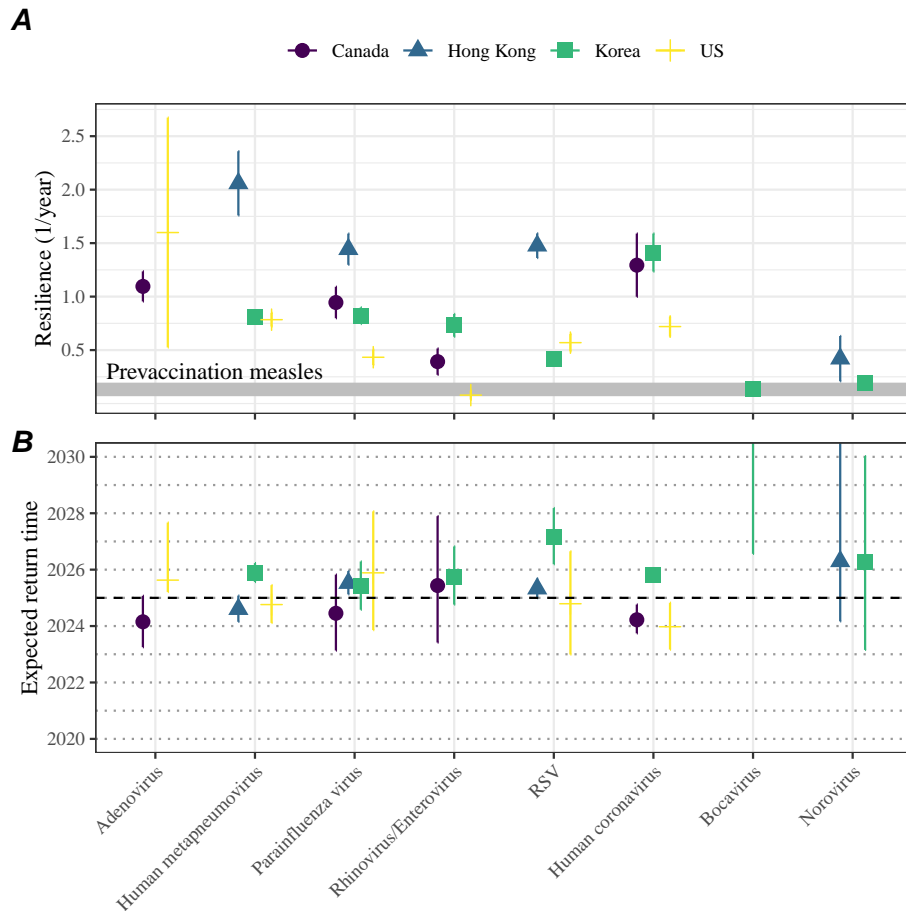


Figure S9: **Predicted timing of when each pathogen will return to their pre-pandemic cycles (zoomed out).** The dashed line in panel B indicates the end of 2024 (current observation time). Error bars represent 95% confidence intervals.



**Figure S10: Estimated time series of distance from attractor for each pathogen across Canada, Hong Kong, Korea, and the US using higher embedding dimensions.** Black lines represent the estimated distance from attractor. Red lines and shaded regions represent the linear regression fits and corresponding 95% confidence intervals. Dashed lines represent the average of the pre-pandemic nearest neighbor distances. A lower threshold is used for determining embedding dimensions with the false nearest neighbors approach, thereby yielding a higher embedding dimension.



**Figure S11: Summary of resilience estimates using higher embedding dimensions.** (A) Estimated pathogen resilience. The gray horizontal line represents the intrinsic resilience of pre-vaccination measles dynamics. (B) Predicted timing of when each pathogen will return to their pre-pandemic cycles. The dashed line in panel B indicates the end of 2024 (current observation time). Error bars represent 95% confidence intervals. A lower threshold is used for determining embedding dimensions with the false nearest neighbors approach, thereby yielding a higher embedding dimension.

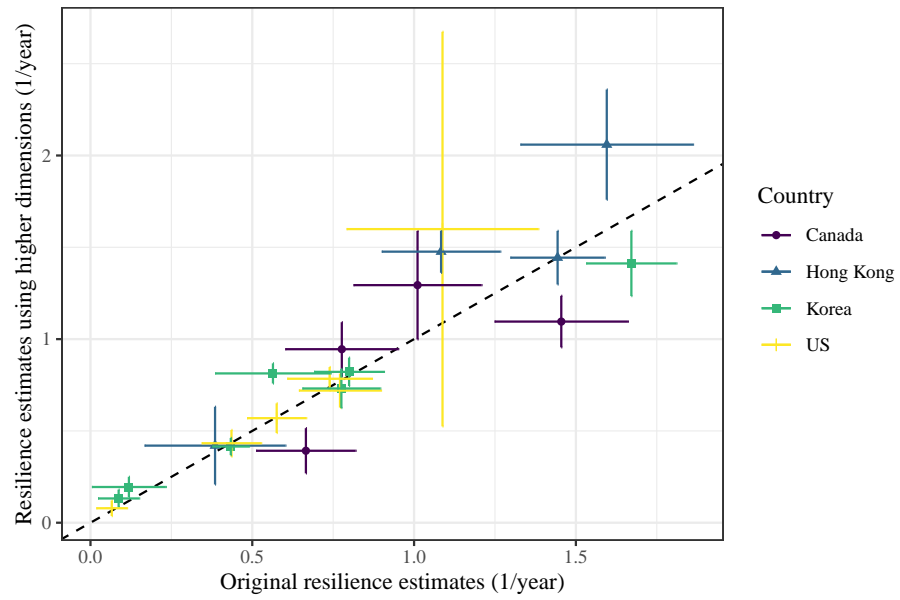


Figure S12: **Comparison of resilience estimates.** Each point represents a resilience estimate for a specific pathogen at a specific country. The x values represent the original resilience estimates presented in Figure 4. The y values represent the original resilience estimates presented in Supplementary Figure S11.

## 658 References

- 659 [1] Rachel E Baker, Sang Woo Park, Wenchang Yang, Gabriel A Vecchi, C Jessica E  
660 Metcalf, and Bryan T Grenfell. The impact of COVID-19 nonpharmaceutical  
661 interventions on the future dynamics of endemic infections. *Proceedings of the*  
662 *National Academy of Sciences*, 117(48):30547–30553, 2020.
- 663 [2] Gabriela B Gomez, Cedric Mahé, and Sandra S Chaves. Uncertain effects of the  
664 pandemic on respiratory viruses. *Science*, 372(6546):1043–1044, 2021.
- 665 [3] Mihaly Koltai, Fabienne Krauer, David Hodgson, Edwin van Leeuwen, Marina  
666 Treskova-Schwarzbach, Mark Jit, and Stefan Flasche. Determinants of RSV  
667 epidemiology following suppression through pandemic contact restrictions. *Epi-*  
668 *demics*, 40:100614, 2022.
- 669 [4] Sang Woo Park, Brooklyn Noble, Emily Howerton, Bjarke F Nielsen, Sarah  
670 Lentz, Lilliam Ambroggio, Samuel Dominguez, Kevin Messacar, and Bryan T  
671 Grenfell. Predicting the impact of non-pharmaceutical interventions against  
672 COVID-19 on *Mycoplasma pneumoniae* in the United States. *Epidemics*,  
673 49:100808, 2024.
- 674 [5] Eric J Chow, Timothy M Uyeki, and Helen Y Chu. The effects of the COVID-19  
675 pandemic on community respiratory virus activity. *Nature Reviews Microbiol-*  
676 *ogy*, 21(3):195–210, 2023.
- 677 [6] Stephen M Kissler, Christine Tedijanto, Edward Goldstein, Yonatan H Grad,  
678 and Marc Lipsitch. Projecting the transmission dynamics of SARS-CoV-2  
679 through the postpandemic period. *Science*, 368(6493):860–868, 2020.
- 680 [7] Rachel E Baker, Chadi M Saad-Roy, Sang Woo Park, Jeremy Farrar, C Jessica E  
681 Metcalf, and Bryan T Grenfell. Long-term benefits of nonpharmaceutical inter-  
682 ventions for endemic infections are shaped by respiratory pathogen dynamics.  
683 *Proceedings of the National Academy of Sciences*, 119(49):e2208895119, 2022.
- 684 [8] Edward A Bender, Ted J Case, and Michael E Gilpin. Perturbation experiments  
685 in community ecology: theory and practice. *Ecology*, 65(1):1–13, 1984.
- 686 [9] Anthony R Ives and Stephen R Carpenter. Stability and diversity of ecosystems.  
687 *science*, 317(5834):58–62, 2007.
- 688 [10] Marten Scheffer, Jordi Bascompte, William A Brock, Victor Brovkin, Stephen R  
689 Carpenter, Vasilis Dakos, Hermann Held, Egbert H Van Nes, Max Rietkerk,  
690 and George Sugihara. Early-warning signals for critical transitions. *Nature*,  
691 461(7260):53–59, 2009.
- 692 [11] Stuart L Pimm. The structure of food webs. *Theoretical population biology*,  
693 16(2):144–158, 1979.

- 694 [12] Michael G Neubert and Hal Caswell. Alternatives to resilience for measuring  
695 the responses of ecological systems to perturbations. *Ecology*, 78(3):653–665,  
696 1997.
- 697 [13] Lance H Gunderson. Ecological resilience—in theory and application. *Annual  
698 review of ecology and systematics*, 31(1):425–439, 2000.
- 699 [14] Vasilis Dakos and Sonia Kéfi. Ecological resilience: what to measure and how.  
700 *Environmental Research Letters*, 17(4):043003, 2022.
- 701 [15] Jeanne C Chambers, Craig R Allen, and Samuel A Cushman. Operationalizing  
702 ecological resilience concepts for managing species and ecosystems at risk.  
703 *Frontiers in Ecology and Evolution*, 7:241, 2019.
- 704 [16] Georgiy V Bobashev, Stephen P Ellner, Douglas W Nychka, and Bryan T  
705 Grenfell. Reconstructing susceptible and recruitment dynamics from measles  
706 epidemic data. *Mathematical Population Studies*, 8(1):1–29, 2000.
- 707 [17] Bärbel F Finkenstädt and Bryan T Grenfell. Time series modelling of childhood  
708 diseases: a dynamical systems approach. *Journal of the Royal Statistical Society  
709 Series C: Applied Statistics*, 49(2):187–205, 2000.
- 710 [18] Floris Takens. Detecting strange attractors in turbulence. In *Dynamical Sys-  
711 tems and Turbulence, Warwick 1980: proceedings of a symposium held at the  
712 University of Warwick 1979/80*, pages 366–381. Springer, 2006.
- 713 [19] Alan Hastings, Karen C Abbott, Kim Cuddington, Tessa Francis, Gabriel Gell-  
714 ner, Ying-Cheng Lai, Andrew Morozov, Sergei Petrovskii, Katherine Scran-  
715 ton, and Mary Lou Zeeman. Transient phenomena in ecology. *Science*,  
716 361(6406):eaat6412, 2018.
- 717 [20] Matthew B Kennel, Reggie Brown, and Henry DI Abarbanel. Determining  
718 embedding dimension for phase-space reconstruction using a geometrical con-  
719 struction. *Physical review A*, 45(6):3403, 1992.
- 720 [21] Eugene Tan, Shannon Algar, Débora Corrêa, Michael Small, Thomas Stemler,  
721 and David Walker. Selecting embedding delays: An overview of embedding  
722 techniques and a new method using persistent homology. *Chaos: An Interdis-  
723 ciplinary Journal of Nonlinear Science*, 33(3), 2023.
- 724 [22] Samit Bhattacharyya, Per H Gesteland, Kent Korgenski, Ottar N Bjørnstad,  
725 and Frederick R Adler. Cross-immunity between strains explains the dynamical  
726 pattern of paramyxoviruses. *Proceedings of the National Academy of Sciences*,  
727 112(43):13396–13400, 2015.

- 728 [23] Bryan T Grenfell, Ottar N Bjørnstad, and Bärbel F Finkenstädt. Dynamics of  
729      measles epidemics: scaling noise, determinism, and predictability with the TSIR  
730      model. *Ecological monographs*, 72(2):185–202, 2002.
- 731 [24] Virginia E Pitzer, Cécile Viboud, Vladimir J Alonso, Tanya Wilcox, C Jessica  
732      Metcalf, Claudia A Steiner, Amber K Haynes, and Bryan T Grenfell. Environmental  
733      drivers of the spatiotemporal dynamics of respiratory syncytial virus in  
734      the United States. *PLoS pathogens*, 11(1):e1004591, 2015.
- 735 [25] Katharine R Dean, Fabienne Krauer, Lars Walløe, Ole Christian Lingjærde, Bar-  
736      Barbara Bramanti, Nils Chr Stenseth, and Boris V Schmid. Human ectoparasites  
737      and the spread of plague in Europe during the Second Pandemic. *Proceedings  
738      of the National Academy of Sciences*, 115(6):1304–1309, 2018.
- 739 [26] Margarita Pons-Salort and Nicholas C Grassly. Serotype-specific immunity  
740      explains the incidence of diseases caused by human enteroviruses. *Science*,  
741      361(6404):800–803, 2018.
- 742 [27] Sarah Cobey and Edward B Baskerville. Limits to causal inference with state-  
743      space reconstruction for infectious disease. *PloS one*, 11(12):e0169050, 2016.
- 744 [28] Edward Goldstein, Sarah Cobey, Saki Takahashi, Joel C Miller, and Marc Lip-  
745      sitch. Predicting the epidemic sizes of influenza A/H1N1, A/H3N2, and B: a  
746      statistical method. *PLoS medicine*, 8(7):e1001051, 2011.
- 747 [29] Bob Carpenter, Andrew Gelman, Matthew D Hoffman, Daniel Lee, Ben  
748      Goodrich, Michael Betancourt, Marcus A Brubaker, Jiqiang Guo, Peter Li,  
749      and Allen Riddell. Stan: A probabilistic programming language. *Journal of  
750      statistical software*, 76, 2017.
- 751 [30] Stan Development Team. RStan: the R interface to Stan, 2024. R package  
752      version 2.32.6.